Enhancing Global-Scale Urban Land Cover Representation Using Local Climate Zones in the Community Earth System Model

Yuan Sun[1], Keith W. Oleson[2], Lei Zhao[3,4,5], Gerald Mills[6], Cenlin He[7], Matthias Demuzere[8], David O. Topping[1], Ning Zhang[9,10], Zhonghua Zheng[1]

[1]Department of Earth and Environmental Sciences, The University of Manchester, Manchester M13 9PL, UK
[2]Climate and Global Dynamics Laboratory, NSF National Center for Atmospheric Research, Boulder, CO 80307, USA
[3]Department of Civil and Environmental Engineering, University of Illinois Urbana-Champaign, Urbana, IL 61801, USA
[4]National Center for Supercomputing Applications, University of Illinois Urbana-Champaign, Urbana, IL 61801, USA
[5]Institute for Sustainability, Energy, and Environment, University of Illinois Urbana-Champaign, Urbana, IL 61801, USA
[6]School of Geography, University College Dublin, Dublin, Ireland
[7]Research Applications Laboratory, NSF National Center for Atmospheric Research, Boulder, CO, USA
[8]B-Kode VOF, Ghent, Belgium
[9]School of Atmospheric Sciences, Nanjing University, Nanjing, China
[10]Key Laboratory of Urban Meteorology, China Meteorological Administration, Beijing, China

Key Points:

- We developed a modular approach for implementing an LCZ-based urban land cover representation in CESM.
- Simulations at 20 flux tower sites showed the effectiveness of urban climate modeling using the LCZ scheme.
- Modeled sensible heat flux showed comparable sensitivity to LCZ morphological and thermal parameters.

Corresponding author: Zhonghua Zheng, zhonghua.zheng@manchester.ac.uk

Corresponding author: Ning Zhang, ningzhang@nju.edu.cn

Abstract

Urban areas are increasingly vulnerable to the impacts of climate change, necessitating accurate simulations of urban climates in Earth system models (ESMs) in support of large-scale urban climate adaptation efforts. ESMs underrepresent urban areas due to their small spatial extent and the lack of detailed urban landscape data. To enhance the accuracy of urban representation, this study integrated the local climate zones (LCZs) scheme within the Community Earth System Model (CESM) to better represent urban heterogeneity. We adopted a modular approach to incorporate the ten built LCZ classes into CESM as a new option in addition to the default urban three-class scheme (i.e., tall building district, high density, and medium density). CESM simulations using the LCZ-based urban characteristics were validated globally at 20 flux tower sites, showing site-averaged improvement in modeling upward longwave radiation (LW_{up}) and anthropogenic heat flux (Q_{ahf}), but increased uncertainties in modeling sensible heat flux (Q_h). The root-mean-square error between the observed and simulated Q_{ahf} using the LCZ decreased by 4% compared to using the default. Model sensitivity experiments revealed that LW_{up} and Q_h had comparable sensitivity to LCZ urban morphological and thermal parameter subsets. This study assessed and demonstrated the implementation as the starting point for future work on better resolving urban areas in Earth system modeling.

Plain Language Summary

Cities worldwide are diverse in their land covers, morphological patterns, material properties, and human activities, all affecting urban climate. However, most Earth system models oversimplify city landscapes or ignore them altogether, limiting their ability to accurately simulate urban climates. This study aims to improve the representation of urban land covers in the Community Earth System Model (CESM) on a global scale by implementing a more detailed urban classification using the local climate zones (LCZs). Compared to the default urban three-class scheme of CESM (i.e., tall building district, high density, and medium density), the LCZ scheme categorizes built landscapes into one of ten classes. CESM simulations using LCZ-derived urban parameters were compared with observations at 20 flux tower sites. The results showed site-averaged improvements in simulated upward longwave radiation and anthropogenic heat fluxes but also more uncertainties in modeling sensible heat flux. The findings also illuminated the need to develop more detailed urban parameter datasets.

1 Introduction

Urban climate varies across urban landscapes, shaped by the spatial heterogeneity of land cover, including the arrangement of buildings, roads, and vegetation. These variations are closely associated with specific land uses (e.g., industry, residential, or commercial). Urban land cover and land use influence local biogeophysical and biogeochemical processes such as surface energy exchange (Kotthaus & Grimmond, 2014) and urban greening (L. Li et al., 2023), as well as hydrological cycles (Fletcher et al., 2013). Despite their relatively small footprint, urban areas also contribute disproportionately to global anthropogenic emissions owing to the concentration of human activities (Hansen & Stone, 2016). However, precisely representing urban areas for quantitative research remains challenging, with one of the major hurdles being a consistent way of describing diverse urban landscapes both within and across cities. To better capture these complexities, Stewart and Oke (2012) introduced the local climate zone (LCZ) classification scheme, primarily as a framework for studying the canopy-level urban heat island. This framework, which consists of ten built types and seven natural land cover types, provides a typology of urban neighborhoods that is universal in scope and each is associated with a range of climate-relevant urban parameters, including building height, surface cover, and radiative and thermal properties (Ching et al., 2018).

The LCZ scheme is now a widely adopted approach in urban climate research and adaptation planning (e.g., Aslam & Rana, 2022; Huang et al., 2023; H. Zhang et al., 2024). For instance, Gilabert et al. (2021) demonstrated that the relative risk of mortality in Barcelona increased by 80% on days where temperatures were in the 90th percentile, with risk varying across different LCZs. This refined understanding of heat risks was supposed to help urban planners and policymakers anticipate and mitigate the effects of climate change, promoting more resilient and sustainable urban environments. Furthermore, more than ten numerical meso- and micro-scale models have incorporated LCZs into their urban land cover representation and parameterization schemes (Table 1). Numerical simulations used LCZ maps to represent land covers, distinguishing between built and natural classes. Early applications of LCZ maps and corresponding parameters in numerical simulations were pioneered by Stewart et al. (2014), further developed by Middel et al. (2014) and P. J. Alexander et al. (2015). They conducted single-point simulations on a building scale using urban models such as the Town Energy Balance (TEB) model, ENVI-met, and the Surface Urban Energy and Water Balance Scheme (SUEWS). These studies demonstrated improved performance in capturing surface energy balance variations across different urban landscapes. LCZs were later integrated into more complex land surface models and regional climate models, enabling grid-based approaches to represent larger urban areas. This transition has expanded analysis from the building scale to the city scale, with land surfaces resolved at grid resolutions ranging from 0.1 km (e.g., Verdonck et al., 2018) to 1 km (e.g., Brousse et al., 2020; Cui et al., 2023). Larger-scale simulations using regional climate models have facilitated the study of urban climate phenomena over broader spatial extents and enabled the ability to simulate interactions between diverse urban forms and regional climate systems. The integration of LCZs in the widely-used Weather Research and Forecasting (WRF) model has shown promise for mesoscale simulations (e.g. Du et al., 2023; Molnár et al., 2019; Patel et al., 2020; Pellegatti Franco et al., 2019). For instance, Brousse et al. (2016) found that simulations using WRF with LCZs exhibited more consistent trends in canopy-level (2 m air) temperature and above-canopy wind variations in Madrid, compared to the default data with only three urban classes. Similarly, a case study in Mumbai demonstrated improved performance in simulating heavy rainfall when using WRF with LCZs (Patel et al., 2020). However, some studies have identified uncertainties introduced by LCZs. Liang et al. (2021) reported that simulated urban 2 m air temperature at 20 weather stations of Beijing using WRF with LCZs showed a higher bias (1.94°C) compared to simulations using default land surface data with a single urban class (1.32°C). This bias could be mitigated by incorporating localized emissivity and albedo values for urban parameters within the LCZs, demonstrating the need for accurate LCZ-dependent parameters.

Table 1. Timeline of incorporating LCZ-based land-cover representation in numerical models.

Year of first incorporation	Urban model	Land surface model	Climate model	Case study area	Urban climate scale	LCZs mapping method	LCZ map resolution	Urban/land model grid-spacing	Later studies
Stewart et al. (2014)	Town Energy Balance (TEB)	None	None	3 cities (Nagano, Vancouver, Uppsala)	Micro	Fieldwork and visual inspection	Single-point (0.1–0.2 km radius)	–	e.g., Kwok et al. (2019); Cui et al. (2023)
Middel et al. (2014)	ENVI-met	None	None	1 city (Phoenix)	Micro	Fieldwork	Single-point (0.1–0.12 km in length)	0.001 km	e.g., Lyu et al. (2019); Unal Cilek and Cilek (2021); Kwok et al. (2019)
P. J. Alexander et al. (2015)	Surface Urban Energy and Water Balance Scheme (SUEWS)	None	None	1 city (Dublin)	Local	Fieldwork and remote sensing	Single-point (1 km^2)	–	P. Alexander et al. (2016); Fernández et al. (2021); Obe et al. (2024)
Brousse et al. (2016)	Building Effect Parameterization and Building Energy Model (BEP–BEM)	Noah Land Surface Model	Weather Research and Forecasting (WRF) model	1 city (Madrid)	Meso	WUDAPT	Unknown	0.33 km	e.g., Hammerberg et al. (2018); Molnár et al. (2019); Ribeiro et al. (2021); Zhou et al. (2022)
Verdonck et al. (2018)	Urban boundary layer climate model (UrbClim)	Land Surface Interaction Calculation (LAIca)	None	4 cities (Augsburg, Antwerp, Brussels, Ghent)	Meso	WUDAPT	0.1 km	0.1 km	e.g., Caluwaerts et al. (2020); Gilabert et al. (2021); Hidalgo-García and Rezapouraghdam (2023)
Geletič et al. (2018)	Mikroskaliges Urbanes KLImaMOdell in 3-Dimensionen (MUKLIMO_3)	None	None	1 city (Brno)	Meso	GIS-based method	0.1 km	0.1 km	e.g., Geletič et al. (2019); Kwok et al. (2019); Hürzeler et al. (2022)
Kwok et al. (2019)	TEB	SURFace Externalis´ ee (SURFEX) land surface model	MésoNH	1 city (Toulouse)	Meso	GIS-based method	0.1 km	0.25 km	e.g., Kwok et al. (2021)
Brousse et al. (2020)	TERRA_URB	TERRA_ML	COSMO-CLM	1 city (Kampala)	Meso	WUDAPT	0.1 km	1 km	e.g., Kwok et al. (2019); Van de Walle et al. (2021)
Jin et al. (2020)	urban energy balance calculation model (UDC)	None	None	1 city (Guangzhou)	Local	WUDAPT and GIS-based method	Single-point	–	None
Caluwaerts et al. (2020)	Urb-Clim	SURFEX	ALARO	1 city (Ghent)	Meso	WUDAPT	0.1 km	1 km	None
Meili et al. (2021)	Urban Tethys-Chloris (UT&C)	None	None	1 city (Singapore)	Micro	Fieldwork	Single-point (0.15 km radius)	–	None
Moradi et al. (2022)	Vertical City Weather Generator (VCWG)	None	None	1 city (Vancouver)	Micro	Experimental assumption	Single-point	–	None
Xu et al. (2022)	Urban Weather Generator (UWG)	None	None	2 cities (Guangzhou, Nanning)	Local	Fieldwork	Single-point (0.3 km radius)	–	e.g., Maracchini et al. (2023); Xu et al. (2023); Yin et al. (2024)
Cui et al. (2023)	TEB	SURFEX	ALARO	1 cities (Beijing)	Mesco	WUDAPT	0.1 km	1 km	Cui et al. (2024)
C. Li et al. (2023)	Community Land Model Urban (CLMU)	Community Land Model version 5 (CLM5)	None	1 city (Nanjing), 1 region (East China)	Micro, meso	WUDAPT	Single-point (1 km radius), regional (0.1 km)	Single-point (–), Regional (1°)	None

1 A single-point simulation refers to a simulation focused on a single grid cell within an urban domain, as opposed to simulations covering multiple grid cells across cities or regions.

2 "–" denotes that urban representation is not resolved on grid-based data.

3 The classification of urban climate scales refers to Oke et al. (2017) with typical horizontal length ranges: micro (10–200 m), local (0.5–2 km), and meso (25–100 km).

Over the past decade, LCZ-based urban representation in numerical models has evolved markedly, in tandem with improvements in mapping the LCZ types across cities. Initially, LCZ mappings using fieldwork and visual inspection were used to support simulations on case-study urban domains. Recent advancements in GIS and satellite technology and tools have enabled consistent and large-scale mapping of LCZs. The World Urban Database and Access Portal Tools (WUDAPT) project (Ching et al., 2018) has developed a protocol for LCZ mapping that has resulted in global (Demuzere, Kittner, et al., 2022), Europe (Demuzere et al., 2019), and U.S. (Qi et al., 2024) products; each LCZ map is also a map of urban parameters used for classification. This development reflects a growing recognition of the need for detailed urban classification to better understand and address bi-directional effects between urban land and climates. Despite these advancements, however, challenges still remain. Many local and regional urban climate studies adopting LCZs focused on specific cities or regions, employing diverse approaches in model configurations, parameter settings, and physical schemes. While globally consistent LCZ maps have improved the representation of urban land cover, variability persists in how researchers define LCZ urban parameters and set up models. These discrepancies make it difficult to directly compare findings across studies or effectively transfer climate knowledge from one urban region to another.

Recently, global climate models (GCMs) or Earth System Models (ESMs) have been extensively used to simulate urban climates on large spatial scales, ranging from continental to global domains (D. Li et al., 2016; Oleson, Bonan, Feddema, Vertenstein, & Grimmond, 2008; L. Zhao et al., 2021; Zheng et al., 2021). Unlike regional climate models, which focus on localized domains, GCMs/ESMs provide a unified framework for urban climate simulations on a global scale. This unified approach ensures consistent model structures and configurations, enabling robust intercomparisons and assessments of urban climate impacts across regions. Such consistency fosters international cooperation and informs the development of climate adaptation strategies that may be transferable to cities worldwide. Additionally, GCMs/ESMs allow for long-term urban climate projections, considering the interactions among different components of the Earth system, which is crucial for assessing the impacts of adaptive actions on both local and global climates. However, the current treatment of urban areas in GCMs/ESMs limits their ability to capture fine-scale processes but integrating the LCZ classification could improve simulations of interactions between the atmosphere and diverse urban landscapes (Demuzere, Kittner, et al., 2022). This development is needed to meet the demand for urban climate adaptation and is aided by the availability of global LCZ maps and improved computing technology. In this context, C. Li et al. (2023) has represented urban areas in East China with LCZ urban classes in the Community Land Model version 5 (CLM5) (Lawrence et al., 2019), the land component of the Community Earth System Model (CESM) (Danabasoglu et al., 2020), showcasing the potential of LCZs for simulating urban climate in GCMs/ESMs. While previous studies have mainly focused on regional impacts, few studies have explored the broader implications of integrating LCZ-refined urban land cover representation into urban climate modeling across different regions or examined the sensitivity of GCMs/ESMs to LCZ-derived urban parameters.

This study addresses two critical questions: (i) Can incorporating the LCZ classification into the CESM improve urban climate simulations; and (ii) how sensitive is the model to uncertainties in LCZ-derived urban parameters under diverse climate conditions? To answer these questions, we first developed a modular approach to integrating LCZ representation into CESM, specifically within its land component, CLM5. This integration involved modifying the main codebase and adding a new namelist "use_lcz", supporting version control, and facilitating future model improvements and refinements. Second, we assessed model performance at 20 urban flux tower sites worldwide, using parameters from different sources, including the default urban parameter dataset, LCZ urban parameter table from WRF, LCZ table from C. Li et al. (2023), and our newly developed LCZ table. Third, we conducted experiments at three sites, each representing different climate conditions, to assess the sensitivity of the model to the uncertainty of urban parameters by introducing perturbations to an LCZ look-up table. These findings aim to establish a foundation for incorporating LCZ-based urban representation in CESM and other GCMs/ESMs for future global urban climate simulations.

This paper is structured as follows. Section 2 outlines the method and data used to incorporate the built LCZ representation in CESM, including the workflow for model modifications, configuration details, and the setup for single-point simulations in a land-only mode. Section 3 illustrates the model validation results from single-point simulations across 20 urban flux tower sites worldwide, with model outputs compared to observation data. In Section 4, we discuss the results of model sensitivity to perturbed parameters, examining uncertainties associated with four subsets of urban parameters: morphological, radiative, thermal, and indoor parameters. Finally, Section 5 summarizes the key findings and provides insights into future LCZ-based parameter development, and the implications for urban planning and climate policy to enhance adaptation strategies.

2 Model and simulations

This section describes the urban representation hierarchy in CESM and details the modifications made to incorporate the built LCZ typology (Section 2.1). We highlight the technical innovations in the model configuration and the scientific contributions of our simulations, differentiating them from the work of C. Li et al. (2023) (Section 2.2). Next, we describe the validation process, where single-point simulation outputs from the land model are compared with observational data from 20 flux tower sites (Section 2.3). Following this, we explain the setup for sensitivity tests to explore uncertainties introduced by urban parameters (Section 2.4).

2.1 Representing built local climate zone in CESM

CESM is a state-of-the-art global community Earth system model developed by the NSF National Center for Atmosphere Research (NCAR), USA. It consists of seven components: atmosphere, land, ocean, river, land-ice, sea-ice, and ocean-wave (Figure 1(a)). The land model in CESM is the Community Land Model (CLM), which classifies land into five types: vegetated, glacier, crop, lake, and urban, using a sub-grid tiling approach to capture surface details for some of these classes (Figure 1(b)). The urban model within CLM, known as the Community Land Model Urban (CLMU), explicitly represents and parameterizes urban surfaces (Oleson & Feddema, 2020). CLMU is a single-layer urban canopy model that simulates the surface energy and water budget, such as radiative transfer, heat conduction through walls, roofs, and roads, and turbulent heat fluxes (Masson, 2000). It also incorporates a building energy model for heating and air conditioning systems (X. C. Li, Zhao, Oleson, et al., 2024). CLMU has been widely applied in large-scale studies of urban heat (e.g., Yang et al., 2023; K. Zhang et al., 2023; L. Zhao et al., 2014, 2021; Zheng et al., 2021), urban runoff (Gray et al., 2023), urban air conditioning adoption (X. C. Li, Zhao, Oleson, et al., 2024; X. C. Li, Zhao, Qin, et al., 2024), and urban climate adaptation (Sun et al., 2024; J. Zhang et al., 2016). Detailed descriptions of this physical-process-based urban modeling are available in the CLM5 technical documents (Lawrence et al., 2019; Oleson et al., 2010).

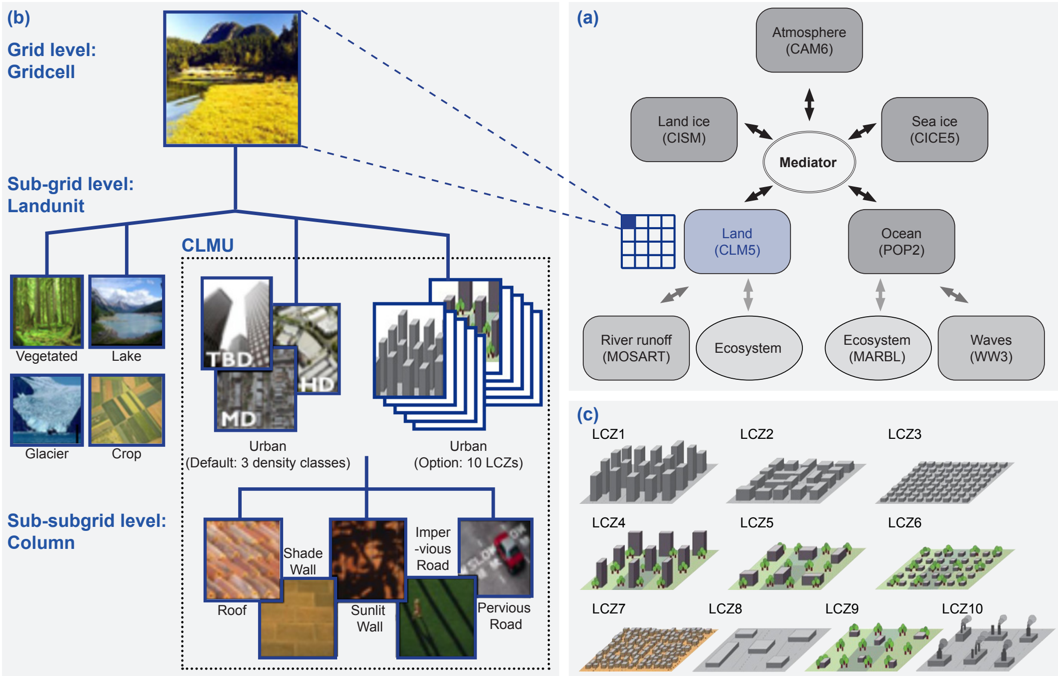

Figure 1. Community Land Model version 5 (CLM5) representation hierarchy with default urban density classes and newly-added built LCZ classes. (a) Community Earth System Model version 2 (CESM2) component structure. (b) The representation hierarchy of CLM5 land surface from the grid, sub-grid, to sub-subgrid levels. (c) Morphology of ten built LCZ classes.

To represent urban complexity, the default CLMU employs a two-level structure. First, at the sub-grid level, urban landunits are divided into three classes: tall building district (TBD), high density (HD), and medium density (MD). These classes were initially introduced by Jackson et al. (2010), who derived a global urban land cover dataset from the LandScan population density data (Dobson et al., 2000) representing conditions for circa-2004. The parameter PCT_URBAN quantifies the percentage of urban area within each urban landunit class. Second, at the sub-subgrid level (the subdivision of the sub-grid), CLMU has five urban surface types (the urban columns), including roof, sunlit wall, shaded wall, pervious canyon floor, and impervious canyon floor. This explicit representation requires over 28 urban parameters (Table 2), covering various aspects including morphological, radiative, thermal, and indoor characteristics. The standard surface inputs adopt the urban parameter dataset of Jackson et al. (2010) as the default, with the updates from Oleson and Feddema (2020).

The main modification of integrating the LCZ into CLMU was made at the sub-grid level, where the LCZ framework was introduced as an alternative to the default three-class urban landunit representation. This followed the standard system proposed by Stewart and Oke (2012), which included ten built types: compact highrise (LCZ1), compact midrise (LCZ2), compact lowrise (LCZ3), open highrise (LCZ4), open midrise (LCZ5), open lowrise (LCZ6), lightweight lowrise (LCZ7), large lowrise (LCZ8), sparsely built (LCZ9), and heavy industry (LCZ10) (Figure 1(c)). Note that we excluded natural LCZ types as CESM did not have an explicit representation of urban vegetation due to computational and input data constraints. Consequently, the pervious canyon floor was modeled as bare soil. Water for evaporation could be supplied by all layers of the soil within the urban extent. In CESM, the number of urban landunits (abbreviated as "numurbl") is a parameter that defines urban landunit classes at the sub-grid level. Originally, "numurbl" is a constant with a default value of 3. To incorporate the LCZ classification, we converted "numurbl" to a variable. This change allowed its value to be adjusted based on the "use_lcz" option specified by users in the CLM5 namelist (Figure 2). By adding the "use_lcz" to the "clm_varctl.F90" module, which handles run control variables, users can activate the LCZ scheme by setting "use_lcz = .true." in the namelist. When activated, this sets "numurbl" to 10 in the "Landunit_varcon.F90" (a module containing landunit level variables and routines). The "UrbanParamsType.F90" module then initializes urban parameters at the sub-subgrid level using corresponding surface data. For global simulations, PCT_URBAN can be calculated based on the established LCZ map developed by Demuzere, Kittner, et al. (2022), while for regional simulations, PCT_URBAN can be sourced from either established LCZ maps or user-provided maps. Given that urban parameters required by CESM are more than LCZ-based original urban parameters can supply (Stewart & Oke, 2012), users can refer to existing look-up LCZ urban parameter tables (Table A2, A3) or customized local datasets. Note that look-up tables are a simplification approach to urban parameters omitting variations across "lsmlat", "lsmlon", "numrad", and "nlevurb" dimensions.

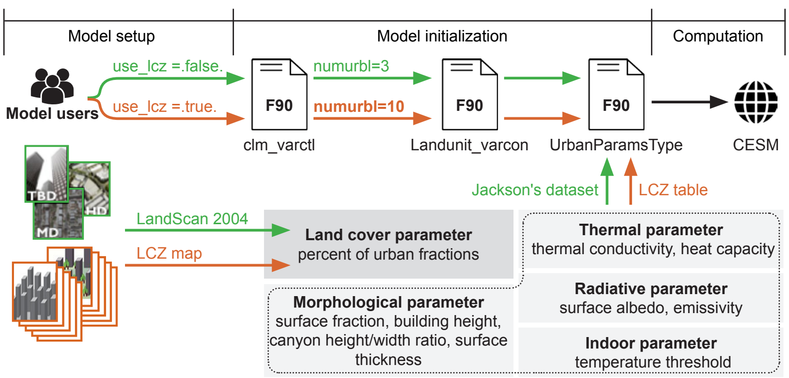

Figure 2. A modular way of incorporating the built LCZ typology alongside the default with their corresponding urban parameters.

Table 2. Urban parameters as inputs in CESM.

Subset	Data dimension	Parameter name	Long name	Unit
Morphological parameters	3 (numurbl, lsmlat, lsmlon)	CANYON_HWR	Canyon height to width ratio	Unitless
		HT_ROOF	Height of roof	meter
		NLEV_IMPROAD	Number of impervious road layers	Unitless
		THICK_ROOF	Thickness of roof	meter
		THICK_WALL	Thickness of wall	meter
		WIND_HGT_CANYON	Height of wind in canyon	meter
		WTLUNIT_ROOF	Fraction of roof	Unitless
		WTROAD_PERV	Fraction of pervious road	Unitless
Radiative parameters	4 (numrad, numurbl, lsmlat, lsmlon)	ALB_IMPROAD_DIF	Diffuse albedo of impervious road	Unitless (range: 0-1)
		ALB_IMPROAD_DIR	Direct albedo of impervious road	
		ALB_PERROAD_DIF	Diffuse albedo of pervious road	
		ALB_PERROAD_DIR	Direct albedo of pervious road	
		ALB_ROOF_DIF	Diffuse albedo of roof	
		ALB_ROOF_DIR	Direct albedo of roof	
		ALB_WALL_DIF	Diffuse albedo of wall	
		ALB_WALL_DIR	Direct albedo of wall	
	3 (numurbl, lsmlat, lsmlon)	EM_IMPROAD	Emissivity of impervious road	
		EM_PERROAD	Emissivity of pervious road	
		EM_ROOF	Emissivity of roof	
		EM_WALL	Emissivity of wall	
Thermal parameters	4 (nlevurb, numurbl, lsmlat, lsmlon)	CV_IMPROAD	Volumetric heat capacity of impervious road	J m^{-3} K^{-1}
		CV_ROOF	Volumetric heat capacity of roof	
		CV_WALL	Volumetric heat capacity of wall	
		TK_IMPROAD	Thermal conductivity of impervious road	W m^{-1} K^{-1}
		TK_ROOF	Thermal conductivity of roof	
		TK_WALL	Thermal conductivity of wall	
Indoor parameter	4 (time, numurbl, lsmlat, lsmlon)	T_BUILDING_MAX	Maximum interior building temperature)	K
	3 (numurbl, lsmlat, lsmlon)	T_BUILDING_MIN	Minimum interier building temperature	

1 "numurbl" is defined as the number of urban density classes, functioning to represent urban landunit types. The default numurbl is 3.

2 "lsmlat" and "lsmlon" are defined as the number of latitudes and longitudes of grid cells, respectively.

3 "nlevurb" is defined as the number of layers to represent the actual properties of the roof, wall, and pervious road construction materials. The default nlevurb is 10.

4 "numrad" is defined as the number of solar bands. The default numrad is 2.

5 The diffuse and direct albedo values of the same surface are set equal.

2.2 Model configuration and simulation description

In the CNTL simulation, we set "use_lcz=.false." into the namelist at the model setup stage to initialize the urban parameters from the default land surface data. In the rest of the simulations, we set "use_lcz=.true." with different LCZ-based land surface inputs. All simulations used a land-only component set `2000_DATM%1PT_CLM50%SP_SICE_SOCN_SROF_SGLC_SWAV` in CESM, activating only CLM5 and excluding other CESM components. Simulations were initialized from a cold state, meaning no prior conditions were assumed (see CLMU technical description Section 1.2.1 (Oleson et al., 2010)), within a grid cell at 20 urban flux tower sites (Figure A1). Simulation periods varied by site, each including a 10-year spin-up period, followed by an analysis period for comparing simulation outputs to quality-controlled observation data provided by the Urban-PLUMBER project (M. Lipson et al., 2022a, 2022b; M. J. Lipson et al., 2023). For instance, at AU-Preston, the atmospheric forcing spanned from 1 January 1993 to 28 November 2004.

This period included a spin-up phase from 1 January 1993, to 12 August 2003, using ERA5-derived atmospheric forcing, and a comparative analysis phase from 12 August 2003, to 28 November 2004, using tower-based observations as atmospheric forcing. The atmospheric forcing inputs, sourced from the same dataset, included eight variables: observational height, precipitation, wind, pressure, specific humidity, temperature, and downward shortwave and longwave radiation. Wind, pressure, specific humidity, and temperature variables were measured at the lowest atmosphere level, typically at observation heights specified in the metadata. Most sites had a 30-minute time interval for atmospheric forcing, except for the JP-Yoyogi, PL-Lipowa, PL-Narutowicza, and US-Baltimore sites, which had a 60-minute interval.

Table 3. Simulation Summary.

Target	Simulation name	Source of urban parameters	Urban landunit classification and land-cover map
Model validation at 20 flux tower sites	CNTL	Urban-PLUMBER project (M. Lipson et al., 2022b) and the default urban parameters	One dominant urban landunit class: medium-density (MD)
	WRF_LCZ	Urban-PLUMBER project and WRF's LCZ urban parameter table (`https://github.com/wrf-model/WRF/blob/master/run/URBPARM_LCZ.TBL`, Table A2)	10 built LCZ classes using 100 m global LCZ map (Demuzere, Kittner, et al., 2022)
	LI_LCZ	Urban-PLUMBER project and C. Li et al. (2023)'s LCZ urban parameter table (Table A2)	
	CESM_LCZ	Urban-PLUMBER project and a newly developed LCZ urban parameter table (Table A3)	
Model sensitivity test over three flux tower sites	BASE	Table A3	
	SENS	An ensemble of simulations, each with a perturbation applied to a subset of parameters from Table A3	

1 All simulations set PCT_URBAN to 100% to focus exclusively on urban climate simulations without including computations for non-urban landunits (i.e., vegetated, lake, glacier, and crop).

2 Model validation simulations (i.e., CNTL, WRF_LCZ, LI_LCZ, and CESM_LCZ) used morphological parameters and albedo parameters provided by the Urban-PLUMBER project.

3 The CNTL simulation assumed that all Urban-PLUMBER sites were categorized as medium-density based on local building height.

4 Given that WRF's LCZ urban parameter table did not provide parameters for impervious roads and interior temperature, we used these missing parameters from LI's table in the WRF_LCZ simulation.

5 Table A3 is a newly developed LCZ urban parameter table derived from the two existing LCZ urban parameter tables. Details on updating LCZ urban parameters are described in Appendix A3.

6 The actual footprints of Urban-PLUMBER flux towers varied, while we used a fixed 500 m radius to extract land cover fractions for consistency.

While C. Li et al. (2023) has made progress in implementing LCZ into CLM5, the work here introduced three key advancements: a modular approach to model modification, an enhanced LCZ urban parameter table, and an investigation into model sensitivity to uncertainties in LCZ urban parameters. Firstly, while C. Li et al. (2023) replaced the default urban representation with the LCZ scheme through the ad-hoc "source modifications" (SourceMods) approach, our study used a modular approach, which avoided the limitations of hard-coding changes. This method integrated LCZs as an alternative representation of urban land cover, alongside the default scheme, within the main structure of the model. The modular approach offered several advantages, including maintaining compatibility with future model developments and facilitating version control. Secondly, the validation conducted by C. Li et al. (2023) was based on a single city, Nanjing, China, using an urban parameter look-up table. In contrast, our study extended this validation by comparing outputs with observations from 20 global flux tower sites from the Urban-PLUMBER project (`https://urban-plumber.github.io`). We also evaluated model performance using a variety of urban parameter datasets, including the default data of CESM and LCZ urban parameter tables (i.e., LCZ urban parameter table from WRF and LCZ urban parameter table from C. Li et al. (2023)) in the CNTL, WRF_LCZ, and LI_LCZ simulations (Table 3). Based on these evaluations, we refined several parameters and developed a new LCZ urban parameter table (Tables A3), which was subsequently used in the CESM_LCZ simulation. Thirdly, we conducted sensitivity tests at three flux tower sites: AU-Preston (Demuzere et al., 2013), US-Baltimore, and US-WestPhoenix, by introducing perturbations to four subsets of urban parameters: morphological, radiative, thermal, and indoor settings. Given that parameters were likely to determine more statistical error than models themselves (Demuzere et al., 2017), sensitivity experiments helped for future parameter dataset development. The perturbation approach built on the work of Oleson, Bonan, Feddema, and Vertenstein (2008), which tested an earlier version of CLMU in CLM3 at two urban sites (Mexico City and Vancouver) and assessed four variables: net radiation, latent heat flux, sensible heat flux, and storage heat flux. Our study advanced this by running the updated CLMU in CLM5 with LCZ urban parameters and examining additional variables such as absorbed solar radiation, upward longwave radiation, momentum flux, and anthropogenic heat flux.

2.3 Single-point simulation for model validation

2.3.1 Land surface input data

Urban parameters used for model validation were derived from two main sources. First, we used the local parameter values provided in the Urban-PLUMBER site data sheet (M. Lipson et al., 2021), which were used for field experiments. These parameters characterized local morphological features including building height, canyon height-to-width ratio, roof fraction, pervious road fraction, and radiative properties such as albedo at each site. Second, beyond the parameters provided by Urban-PLUMBER, several additional parameters (thickness of roof and wall, emissivity, thermal, and indoor settings) required in CLMU were not included in the Urban-PLUMBER dataset. These missing parameters were then sourced from other datasets. CNTL simulation used missing parameters from the medium-density class in the default dataset. This model configuration was consistent with the one submitted as part of the Urban-PLUMBER project (M. J. Lipson et al., 2023). The WRF_LCZ and LI_LCZ simulations represented LCZs at each site and used missing parameters from the two look-up LCZ urban parameter tables, respectively (Table A2). The former used the LCZ urban parameter table (Demuzere, Argüeso, et al., 2022; Zonato et al., 2020), which has been officially incorporated into the WRF model. The latter used LCZ urban parameter table from C. Li et al. (2023), which took the median values of data ranges given by Stewart et al. (2014) and Zonato et al. (2020) for CLM5. As the WRF LCZ table did not provide parameter values for pervious surface and indoor temperature, we used the same values for these as in the LI LCZ table.

2.3.2 Simulation analysis

To conduct model validation, we examined urban surface energy by comparing CLMU outputs in the CNTL, WRF_LCZ, LI_LCZ, and CESM_LCZ simulations with observational data provided by the Urban-PLUMBER project. In CLMU, the urban surface balance equation is (Equation 1):

$$\begin{aligned} R_n &= SW_{down} - SW_{up} + LW_{down} - LW_{up} \\ &= Q_h + Q_{le} + (Q_g - Q_{ac} + Q_{heat} - Q_v) - Q_w - Q_{heat} \\ &= Q_h + Q_{le} + Q_g - Q_{ac} - Q_v - Q_w, \end{aligned} \tag{1}$$

where R_n is net radiation on urban surfaces, calculated as the balance between upwelling and downward radiation fluxes. Specifically, SW_{up} and SW_{down} are upwelling and downward shortwave radiation fluxes. LW_{up} and LW_{down} are upwelling and downward longwave radiation fluxes. The net energy from R_n is then partitioned into ground heat flux and turbulent fluxes. Q_h is upward sensible heat flux, Q_{le} is upward latent heat flux, Q_g is urban heat flux into soil or snow, Q_{ac} is urban air conditioning flux, Q_{heat} is urban heating flux transferred from the indoor to the street canyon, Q_w is sensible heat flux from heating or cooling sources of urban waste heat, and Q_v is ventilation heat flux.

The observational data used for validation primarily included five flux variables: SW_{up}, LW_{up}, Q_h, Q_{le}, and momentum flux (Q_{tau}). Additionally, we examined anthropogenic heat flux (Q_{ahf}) as simulated in CLMU, which accounted for heat generated by building energy use including heating and air conditioning, based on indoor temperature. The building energy model calculates heat flux when the indoor temperature falls below the minimum threshold (T_BUILDING_MIN), which triggers heating, and activates air conditioning when the indoor temperature exceeds the maximum threshold (T_BUILDING_MAX). The modeled Q_{ahf}, which is introduced into the climate system, is calculated as (Equation 2):

$$Q_{ahf} = Q_{heat} + Q_w. \tag{2}$$

We used Taylor diagrams to summarize model performance (Taylor, 2001), displaying normalized standard deviation, Pearson correlation coefficient, and normalized centered root-mean square difference (all dimensionless). The normalized standard deviation (σ) between modeled data and observation at each time step is calculated as (Equation 5):

$$\sigma = \frac{\sigma_y}{\sigma_x} = \frac{\sqrt{\frac{1}{n}\sum_{t=1}^{n}(y_t - \bar{y})^2}}{\sqrt{\frac{1}{n}\sum_{t=1}^{n}(x_t - \bar{x})^2}} = \sqrt{\sum_{t=1}^{n}\frac{(y_t - \bar{y})^2}{(x_t - \bar{x})^2}}, \tag{3}$$

where t index a certain time point within the period indexed through n for comparative analysis, excluding spin-up period. y_t represents a specific flux variable from simulation outputs at time t. x_t is the corresponding variable from the observation data, and $\bar{y}$ and $\bar{x}$ are the means of y_t and x_t, respectively. The correlation coefficient (ρ) is calculated by (Equation 5):

$$\rho = \frac{\sum_{t=1}^{n}(x_t - \bar{x}) \cdot (y_t - \bar{y})}{\sqrt{\sum_{t=1}^{n}(x_t - \bar{x})^2 \cdot \sum_{t=1}^{n}(y_t - \bar{y})^2}}, \tag{4}$$

and the normalized centered root-mean square difference (E') in the Taylor diagrams are interrelated by (Equation 5):

$$E' = \sqrt{\sigma^2 + 1 - 2\sigma \cdot \rho}. \tag{5}$$

Besides statistically summarizing model performance in 20 sites, we also examined the flux fluctuation by calculating the seven-day rolling mean and diurnal mean heat flux with root-mean square error (RMSE) metric (He et al., 2008) for each site (Equation 6):

$$\mathrm{RMSE} = \sqrt{\frac{1}{n}\sum_{t=1}^{n}(y_t - x_t)^2}. \tag{6}$$

We calculated seven-day rolling mean values to smooth out fluctuations in time-series data, reducing noise and short-term variability of the raw data. The diurnal mean helps capture the daily cycle or pattern of diurnal variations.

2.4 Single-point simulations for urban parameter sensitivity

To assess the model sensitivity to urban parameters, we conducted another two simulations (i.e., BASE and SENS) using baseline parameters from the newly developed LCZ urban parameter table (Table A3) and perturbed parameters, respectively. Unlike most previous model sensitivity tests that focused on a single site (e.g., Demuzere et al., 2013, 2017; Tsiringakis et al., 2019; W. Zhao et al., 2014), we selected three sites AU-Preston, US-Baltimore, and US-WestPhoenix to examine if model sensitivity was dependent on background climate. These sites were chosen based on two criteria: (i) they were nearly 100% classified as LCZ6 (open low-rise), ensuring consistency in urban landscape; and (ii) they were situated in temperate, cold, and arid climates, respectively, allowing to explore climate-specific responses.

Model spin-up simulations were conducted for each site, followed by a seven-day simulation for analysis. Simulations started on 18 May 2004 at AU-Preston, 5 December 2006 at US-Baltimore, and 24 December 2012 at US-WestPhoenix, respectively. The chosen simulation periods corresponded to winter at each site, as this was critical for assessing the model sensitivity to indoor minimum building temperatures, which served as the threshold for heating requirements. All simulations at the same site ran in a land-only mode under the same initial conditions, atmospheric forcing, and model configuration, with adjustments to subsets of urban parameters.

We quantified the model sensitivity for four subsets of urban parameters, including six morphological parameters (canyon height to width ratio, height of roof, thickness of roof and wall, fraction of roof and pervious road), eight radiative parameters (albedo and emissivity of impervious road, pervious road, roof, and wall), six thermal parameters (thermal heat capacity and thermal conductivity of impervious road, pervious road, roof, and wall), and one indoor temperature parameter (T_BUILDING_MIN). Morphological parameters, albedo, and thermal parameters were perturbed by ± 20% (Oleson, Bonan, Feddema, & Vertenstein, 2008). Emissivity was perturbed by ± 2%, taking into consideration the physical constraints of emissivity ranging from 0 to 1. T_BUILDING_MIN was perturbed by ± 5%, ± 10%, ± 15%, ± 20%, respectively. Thus, we conducted 2^6=64 SENS simulations for the morphological subset (six parameters with two perturbation factors each), 2^8=256 simulations for the radiative subset, 2^6=64 simulations for the thermal subset, and 8^1=8 simulations for T_BUILDING_MIN, respectively. We excluded model sensitivity to T_BUILDING_MAX, as our simulations have not considered air conditioning adoption yet (X. C. Li, Zhao, Oleson, et al., 2024).

3 Model validation for implementing urban representation with LCZs

Section 3.1 describes the results of the UK-KingsCollege site, providing an example of surface energy variations over time. Section 3.2 compares the observed and modeled variables over all Urban-PLMUBER flux tower sites, with results summarized using Taylor diagrams. Section 3.3 discusses the model performance with LCZs using updated urban parameters.

3.1 Model performance at UK-KingsCollege site

Within the 500 m radius flux tower domain, the UK-KingsCollege site (51.5118°N, 0.1167°W) comprised 77.0% LCZ2 (compact midrise), 16.1% LCZ4 (open highrise), 6.3% LCZ1 (compact highrise), and 0.6% LCZ10 (heavy industry) according the global 100 m LCZ map representing the year of 2018 (Table A1). In addition to parameters provided by Urban-PLUMBER, such as canyon height-to-width ratio, building height, roof fraction, pervious road fraction, and albedo, we used the remaining parameters for each LCZ class from Table A2 in the WRF_LCZ and LI_LCZ simulations. Figure 3 shows the temporal variations in observed and modeled radiative, turbulent, and momentum flux. Additional graphic illustrations for the other sites are available in the repository (`https://github.com/envdes/code_CESM_LCZ`).

Three simulations at this site showed similar patterns of daily and diurnal net radiation (R_n) in line with observations (Figure 3(a)–(b)). There were minimal differences between the two LCZ-based simulations (WRF_LCZ and LI_LCZ), both of which differed from the CNTL simulation. This suggested that the LCZ-based models were relatively insensitive to variations in the thickness of wall and roof, emissivity, and thermal parameters at the UK-KingsCollege site. Since the CNTL, WRF_LCZ, and LI_LCZ simulations all used the same albedo parameters, the modeled upward solar radiation (SW_{up}) exhibited similar temporal trends and magnitudes (Figure 3(c)–(d)), closely matching the observed SW_{up}. However, the seven-day rolling mean modeled upward longwave radiation LW_{up} was consistently higher than observed by 4.3 ± 3.4, 2.5 ± 3.4, and 2.6 ± 3.5 W m^{-2} for the CNTL, WRF_LCZ, and LI_LCZ simulations, respectively (Figure 3(e)). In the CNTL simulation, daytime LW_{up} (06:00–18:00) was higher than observed (Figure 3(f)). The diurnal mean LW_{up} in the CNTL simulation peaked at local 12:30 (419.4 W m^{-2}), earlier than the observed peak at 13:30 (404.8 W m^{-2}). In the WRF_LCZ and LI_LCZ simulations, the diurnal mean LW_{up} was higher than observations by 2.5 ± 0.7, and 2.6 ± 0.9 W m^{-2}, respectively, yielding a lower RMSE. The elevated LW_{up} in the CNTL simulation could be attributed to higher emissivity, with road and wall emissivity set to 0.97–0.99, which was higher than in WRF_LCZ and LI_LCZ simulations.

Compared to radiation variables, turbulent flux variables including sensible heat flux (Q_h) and latent heat flux (Q_{le}) showed greater uncertainties. The modeled Q_h were generally lower than observed values (Figure 3(g)–(h)), particularly during the winter. For instance, on 25 December 2012, Q_h was −8.9 W m^{-2} in the CNTL simulation, whereas in the WRF_LCZ and LI_LCZ simulations were even lower (−15.2 and −13.4 W m^{-2}). Q_h represented the rate of heat transfer between the urban canyon and the atmosphere driven by temperature gradients. Within the urban canyon, the air interacted directly with the roof, wall, and road, as well as was warmed by waste heat due to building heating (Oleson et al., 2010; Oleson & Feddema, 2020). The negative values of modeled Q_h indicated that, in winter, the urban canopy air was cooler than the atmosphere, causing heat to flow from the atmosphere to the urban surfaces. However, this modeled flux was inconsistent with observed values of Q_h, which were positive, indicating upward heat flow. The discrepancies might be attributed to the influence of urban heating in winter. In the CNTL simulation, T_BUILDING_MIN was set to 16.95°C at UK-KingsCollege site, whereas in the WRF_LCZ and LI_LCZ simulations, T_BUILDING_MIN was set to 10°C. The lower T_BUILDING_MIN in the latter two simulations resulted in reduced urban heating and less waste heat. The indoor temperature being equal to T_BUILDING_MIN suggested that the heating threshold was crossed. As a result, the difference in the mean Q_{heat} between the CNTL and WRF_LCZ simulations was 12.6 W m^{-2} while the difference in Q_w was 2.5 W m^{-2}. In the WRF_LCZ simulation, less Q_w was dumped into the urban canyon compared to the CNTL simulation, leading to a lower canyon air temperature. This, in return, led to the difference in Q_h by 6.3 W m^{-2}. In terms of RMSE, the default also performed better than the LCZs in simulating diurnal variations of Q_h. Daytime Q_h in the CNTL simulation was higher in simulations with LCZs (Figure 3(h)). Higher Q_h suggested a higher temperature gradient between the surface and the atmosphere, where urban surfaces represented using default parameters heat up more quickly under solar radiation. At night, simulated Q_h dropped to lower values, where urban surfaces cooled down quickly and retained less heat. Negative nighttime Q_h in the CNTL simulation indicated that urban surfaces radiated heat effectively and cooled down faster than the atmosphere, reversing the temperature gradient from downward to upward.

Besides uncertainties introduced by T_BUILDING_MIN, underestimated momentum flux (Figure 3(k)–(l)) was another factor contributing to reduced turbulent fluxes, where the available energy might be partitioned into ground flux instead. On 25 December 2012, the observed Q_{tau} was 0.4 kg m^{-1} s^{-2} while modeled Q_{tau} was 0.3 kg m^{-1} s^{-2} in all simulations. Momentum flux was controlled in part by the roughness of urban surfaces. According to the assumption of CLMU on roughness length described in Appendix B2, morphological parameters were the same in three simulations, leading to similar roughness length and modeled Q_{tau} values. Additionally, simulated Q_{le} was overestimated in 2013 summer (Figure 3(i)) and during daytime (Figure 3(j)) no matter urban parameter adjustments. Given underestimated Q_h, more energy might be partitioned for evaporation in the model. The use of LCZ urban parameter tables led to a lower RMSE for the diurnal mean Q_{le}, suggesting that applying LCZ urban parameters at the UK-KingsCollege site yields better model performance than using the default MD class parameters.

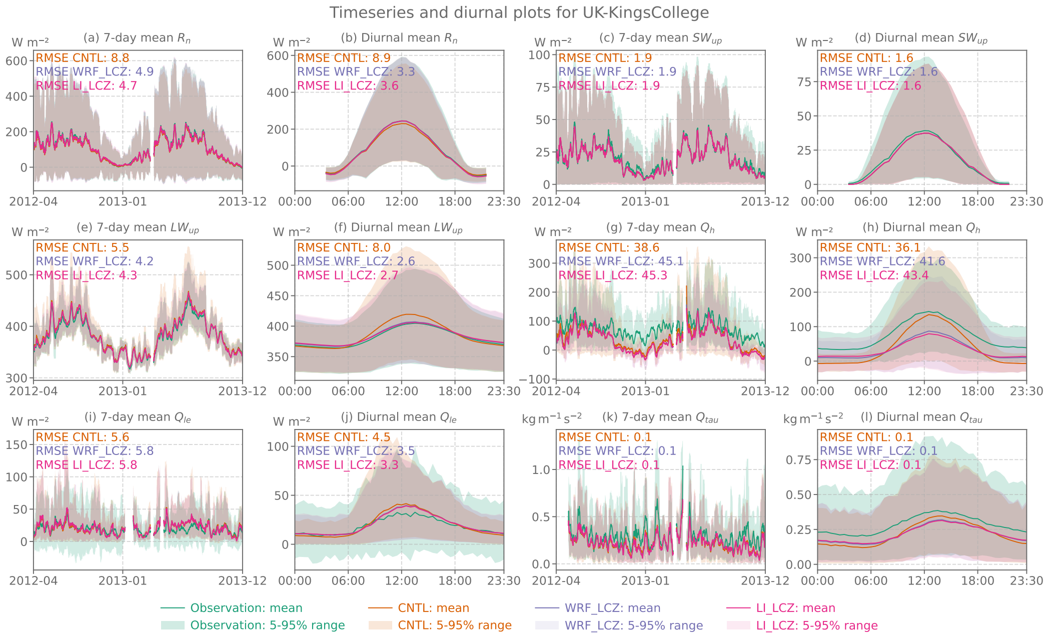

Figure 3. Time-series (UTC time) and diurnal (local time) radiative, turbulent, and momentum flux at the UK-KingsCollege site in the CNTL, WRF_LCZ, and LI_LCZ simulations. (a)–(b) Net radiation on urban surfaces (R_n). (c)–(d) Upward solar radiation (SW_{up}). (e)–(f) Upward longwave radiation (LW_{up}). (g)–(h) Sensible heat flux (Q_h). (i)–(j) Latent heat flux (Q_{le}). (k)–(l) Momentum flux (Q_{tau}). The root-mean-square error (RMSE) measures the average magnitude of the errors between modeled and observed values. Some lines representing the WRF_LCZ and LI_LCZ simulations overlap in the panels.

3.2 Model performance at all Urban-PLUMBER sites

Figure 4 illustrated the performance of simulated radiation, turbulent, and momentum flux for all Urban-PLUMBER sites. Dots of R_n centered around the reference, indicating agreement with observations in the overall energy budget (Figure 4(a)). The normalized standard deviation (σ) of SW_{up} averaged around 1.0 $\pm$ 0.1 across all sites from three simulations (Figure 4(b)). Results from two LCZ-based simulations were very close, with minimal differences resulting from using different thickness of roof and wall, emissivity, volumetric heat capacity, and thermal conductivity parameters from two LCZ urban parameter tables across sites. Some dots representing the CNTL simulation did not overlap with dots from two LCZ simulations, particularly for LW_{up} and Q_h. For LW_{up}, when comparing CNTL, WRF_LCZ, and LI_LCZ simulations to the observational dataset, the σ across all sites averaged at 1.2, 1.1, and 1.1, respectively, all higher than 1 (Figure 4(c)). The maximum σ of LW_{up} occurred at the SG-TelokKurau06 site, located in coastal areas of Singapore, with the σ between the CNTL simulation and observations reaching 2.0. Using parameters from LCZ urban parameter tables narrowed the model deviations for simulating LW_{up} at the SG-TelokKurau06 site, with the σ in the WRF_LCZ and LI_LCZ simulations dropping to 1.6 and 1.7, respectively. Along with overestimated LW_{up}, Q_{le} was underestimated at SG-TelokKurau06, suggesting less energy modeled for evaporation.

The σ of Q_h in the WRF_LCZ simulation averaged at 0.8 $\pm$ 0.1 (Figure 4(d)), 0.2 lower than the σ of Q_h (1.0 $\pm$ 0.2) in the CNTL simulation. The smaller σ of Q_h indicated that using LCZ-based parameters resulted in less variability in Q_h, compared to the observations. This was because the LCZ-based parameters tended to underestimate the diurnal variability of Q_h at most sites, while using the default parameters overestimated the diurnal variability of Q_h at several sites including GR-HECKOR (Figure B1(g)), MX-Escandon (Figure B1(k)), PL-Lipowa (Figure B1(m)), SG-TelokKurau06 (Figure B1(o)), etc. For example, at the GR-HECKOR site, the σ of Q_h in the CNTL simulation was 1.4, which was the largest overestimation of simulated Q_h with the observation across sites, even 0.3 higher than the σ of Q_h in the two LCZ-based simulations. As a result, the day-night difference in Q_h reached 330.1 W m^{-2}, higher than observed day-night difference of 223.6 W m^{-2} (Figure B1(g)). The overestimated Q_h occurred during the daytime, as the default model assumed a larger proportion of the incoming solar energy converted into sensible heat rather than heat stored within the urban fabric. Changes in Q_{le} by using different parameter data were not as much as in Q_h (Figure 4(e)), with the σ of Q_{le} in simulations averaged at 0.9 $\pm$ 0.3. The σ of Q_{tau} among the three simulations varied around 0.4 $\pm$ 0.2 (Figure 4(f)), indicating that the modeled Q_{tau} variations were far smaller than the observed.

Viewed by the correlation coefficient (ρ), most dots representing SW_{up} and LW_{up} gathered within the range between 0.96 and 0.99, indicating a strong positive linear relationship between the modeled and observed radiative variables. However, for turbulent flux variables of Q_h and Q_{le}, the linear relationship was weaker. The ρ of Q_h in three simulations varied from 0.6 to 0.95 and averages at 0.8. For Q_{le}, only a few sites, such as US-Minneapolis2, US-Minneapolis1, and US-Swindon presented relatively high ρ (over 0.8), whereas the rest of the sites showed ρ of simulated Q_{le} varying within a low range. For instance, at GR-HECKOR, ρ of Q_{le} in the CNTL simulation was 0.2, indicating a weak positive relationship between the modeled and observed latent heat fluxes. As ρ mainly primarily reflected how well the temporal patterns of the simulated variables aligned with the observations, changes in urban parameters had little effect on ρ. This is because in the land-only mode, these parameters primarily influence the magnitude of fluxes, not the broader temporal trends, dictated by the atmospheric forcing data.

The centred-root-mean square difference (*E'*) considered both the magnitude and direction of the differences. SW_{up} and LW_{up} generally fell within the contour line of $\pm$ 0.5, indicating close agreement with the observation dataset. As suggested by Oleson, Bonan, Feddema, and Vertenstein (2008), urban net radiation flux was relatively insensitive to uncertainties from thermal parameters compared to morphological and radiative parameters. The agreement between modeled SW_{up} and observation was attributed to prescribing albedo within the flux tower footprint, as solar radiation absorbed or reflected by urban surfaces mainly depended on surface albedo (Akbari et al., 2012). The agreement between modeled LW_{up} and observation resulted from the minimal impacts of changing emissivity, where the range of uncertainties in emissivity was relatively narrow (Artis & Carnahan, 1982). However, there was considerable disagreement for modeled turbulent flux and momentum flux and observed values, where E' varied between the contour line of 0.5 and 1, or even outside of the contour line of 1. At sites such as GR-HECKOR, MX-Escandon, and UK-KingsCollege, the E' of simulated Q_{le} was larger than 1, indicating a significant discrepancy between the simulated and the observed datasets. This was likely due in part to the simplification in modeling urban vegetation in CLMU, where pervious surface was parameterized as bulk soil, lacking urban vegetation-specific evapotranspiration (ET) controls. Uncertainties in modeling Q_{le} were also found in Hertwig et al. (2020)'s simulations using Best et al. (2011)'s one tile scheme and Met Office–Reading Urban Surface Exchange Scheme (MORUSES) without representing non-urban fractions explicitly with vegetation parameterizations at UK-KingsCollege.

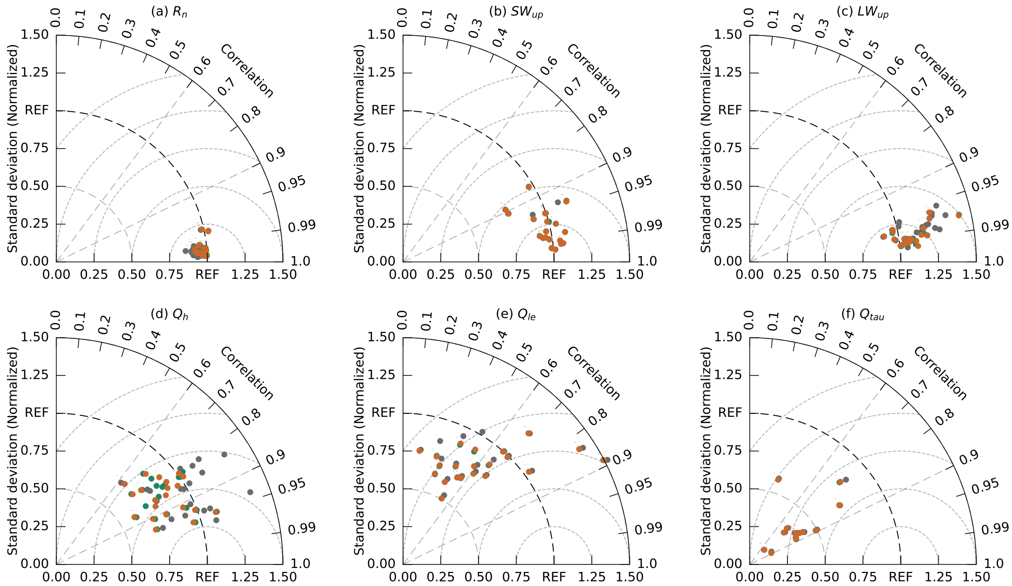

Figure 4. Taylor diagrams showing comparisons between the modeled and observed variables. (a) Net radiation on urban surfaces (R_n). (b) Upward solar radiation (SW_{up}). (c) Upward long-wave radiation (LW_{up}). (d) Sensible heat flux (Q_h). (e) Latent heat flux (Q_{le}). (f) Momentum flux (Q_{tau}). The dots represent sites in the Urban-PLUMBER ensemble, while "REF" denotes the reference dataset from observation. The radial distance between the origin and the symbols represents the normalized standard deviation σ, and the azimuthal position indicates the correlation between modeled data and observed data, with correlation coefficient ρ denoted by the intersection between the radial line and the circle axis. The contours centered on "REF" on the horizontal axis represent E', the normalized centered root-mean square difference.

3.3 Model performance using updated LCZ urban parameters

We compared the annual mean simulated anthropogenic heat flux (Q_{ahf}) to the mean values provided by Urban-PLUMBER, for the AU-Preston site from Best and Grimmond (2016), the FI-Torni site from Dong et al. (2017), the JP-Yoyogi site from Moriwaki et al. (2008), the SG-TelokKurau06 site from Quah and Roth (2012), the UK-KingsCollege and UK-Swindon sites from Ward et al. (2016), as well as other sites from Varquez et al. (2017). Inventory approaches encompass all sources including building, traffic, industry, and metabolism, whereas simulated Q_{ahf} only includes sources from building cooling and space heating. When calculating the annual mean Q_{ahf} from CNTL, WRF_LCZ, and LI_LCZ simulations, we found both underestimation and overestimation of Q_{ahf} across sites (Figure 5(a)). Specifically, CNTL, WRF_LCZ, and LI_LCZ simulations underestimated Q_{ahf} at all sites with temperate climates, and the only site with tropical (the SG-TelokKurau06 site) or arid (the US-WestPhoenix site) climates. For sites with cold climates, the differences between the simulated and provided Q_{ahf} were minimal at FI-Kumpula, KR-Ochang, PL-Lipowa, and PL-Narutowicza sites. However, Q_{ahf} was underestimated at KR-Jungnang, US-Baltimore, and US-Minneapolis2 and overestimated at FI-Torni and US-Minneapolis1. For instance, at KR-Jungnang with a cold climate, Varquez et al. (2017) reported a mean Q_{ahf} as 92.7 W m^{-2}, whereas the annual mean modeled Q_{ahf} averaged at 7.0 W m^{-2} during the simulation period from 24 January 2017 to 29 April 2019 in the CNTL simulation. This underestimation was attributed to single anthropogenic sources of building energy consumption in CLMU. In addition, the averaged error among all sites, quantified by RMSE, reaches 27.7 W m^{-2}. Using the LCZ scheme resulted in RMSE values of 28.9 and 29.0 W m^{-2} in the WRF_LCZ and LI_LCZ simulations, respectively. Higher RMSE occurred when using LCZ urban parameters, possibly due to the simplification of assuming T_BUILDING_MIN at 10°C across LCZ classes. It was a rather low T_BUILDING_MIN compared to the average values in TBD (17.8°C), HD (13.4°C), and MD (13.2°C).

According to Hertwig et al. (2020), the contribution of anthropogenic heat emissions to sensible heat flux was small, but it did influence urban temperature, particularly in autumn and winter. We updated T_BUILDING_MIN in Table A3. For highrises classes (LCZ1 and LCZ4), we increased the T_BUILDING_MIN to 17.85°C to align more closely with the TBD averaged value of 17.8°C. For midrises and lowrises classes (the remaining built-up LCZs), we set T_BUILDING_MIN to 13.85°C, slightly above the average values for HD (13.4°C) and MD (13.2°C), to reduce potential underestimation. Besides T_BUILDING_MIN, we also updated other LCZ urban parameters based on WRF's and LI's LCZ tables (see description in Appendix A3).

CESM_LCZ simulation used albedo and morphological parameters provided by the Urban-PLUMBER and updated LCZ parameters, including the thickness of roof and wall, emissivity, volumetric heat capacity, thermal conductivity, and T_BUILDING_MIN, showing a lower site-averaged RMSE of 26.6 W m^{-2} in Q_{ahf}, with a decrease of 4% compared to the CNTL simulation. The accuracy of simulating Q_{ahf} was related to the background climates. That is, increasing T_BUILDING_MIN in the CESM_LCZ simulation reduced the Q_{ahf} underestimation at sites with temperate, tropical, and arid climates but also aggravated the overestimation at some sites with cold climates. Improvements in other heat flux variables across the three LCZ simulations were very minimal (Figure 5(b)). This indicated that the model showed limited insensitivity to variations in parameters derived from different LCZ tables. Notably, compared to the CNTL simulation, all three LCZ simulations showed larger discrepancies in Q_h. This was evidenced by a lower σ of the Q_h. For diurnal variability, the use of LCZ urban parameters reduced the simulated variability in Q_h at most sites excepted for KR-Ochang (Figure B1(j)) and US-Minneapolis2 (Figure B1(t)). With the same morphological parameters and albedo, the diurnal fluctuations of Q_h using the default thermal parameters were larger than those using LCZ urban thermal parameters, contributing to greater urban surface variability between day and night. Uncertainties in Q_h variability likely arose from the current reliance on a simplified look-up table approach for LCZ urban parameters, with a single value representing the average thermal properties in the "nlevurb" dimension. This contrasted with the default dataset, which explicitly resolved thermal properties across ten layers (Oleson & Feddema, 2020).

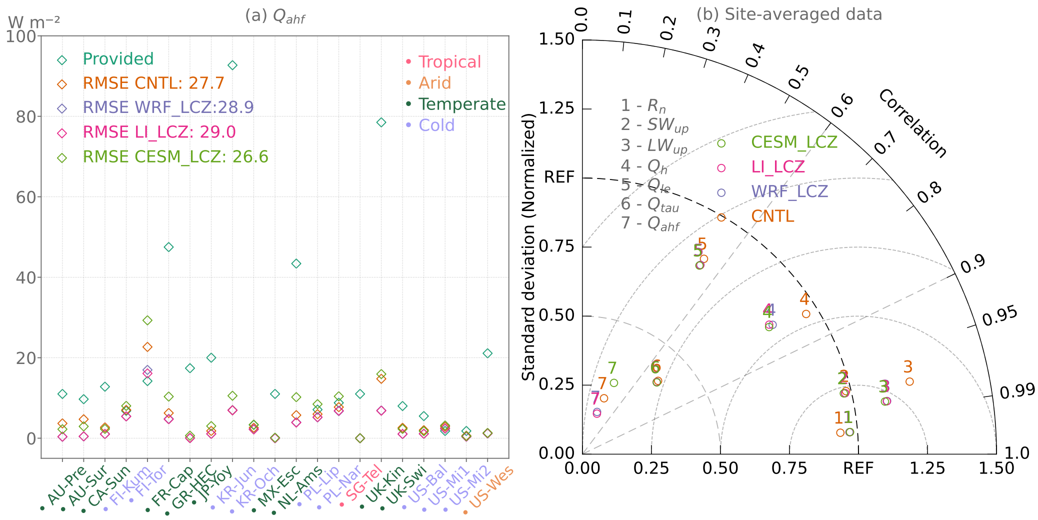

Figure 5. Model performance in CNTL, WRF_LCZ, LI_LCZ, and CESM_LCZ simulations among all Urban-PLUMBER sites. (a) Annual mean anthropogenic heat flux (Q_{ahf}). The root-mean-square error (RMSE) measures the average magnitude of the errors between annual-mean modeled Q_{ahf} and values provided by the Urban-PLUMBER project based on previous studies. The simulation period is more than one year at most sites except for AU-SurreyHills (from 23 February 2004 to 19 July 2004) and SG-TelokKurau06 (from 30 April 2006 to 31 March 2007), so that the mean Q_{ahf} for these two sites is not the exact annual mean. The tick labels on the horizontal axis denote the sites with corresponding background climates. (b) Comparisons between the modeled and the observed variables averaged over sites.

4 Model sensitivity to urban parameter uncertainties

Besides simulations for model validation, we further conducted the sensitivity analysis on urban parameters from the newly developed LCZ urban parameter table (Table A3). Taylor diagrams (Figure 6) summarized the results of four parameter subsets over three flux tower sites of AU-Preston, US-Baltimore, and US-WestPhoenix.

Similar to the findings in Oleson, Bonan, Feddema, and Vertenstein (2008), our results showed that changes in morphological parameters brought the least variability in radiation flux of SW_{up} and LW_{up}, followed by Q_{le}, Q_h, and Q_{tau}. Among six morphological parameters, the σ of Q_h closer to 1 mainly appeared in simulations with -20% roof fraction and -20% canyon height-to-width ratio, indicating that roof fraction and canyon height-to-width ratio played a dominant role in modeling Q_h. Momentum flux was also sensitive to morphological parameters. Taking US-WestPhoenix as an example, the σ of Q_{tau} varied from a minimum of 0.3 to a maximum of 0.6, mainly depending on the roof fraction, and then the building height. The σ of Q_{tau} in 32 simulations with -20% roof fraction was higher than the baseline. According to Equation B5 and Table B2, decreasing roof fraction led to smaller displacement height but larger roughness length, which increases modeled Q_{tau}. Besides roof fraction, modeled Q_{tau} in simulations with $+20\%$ building height was higher than the rest of simulations with -20% building height. As increasing building height increased displacement height and roughness length at the same time, Q_{tau} was less sensitive to building height than to roof fraction.

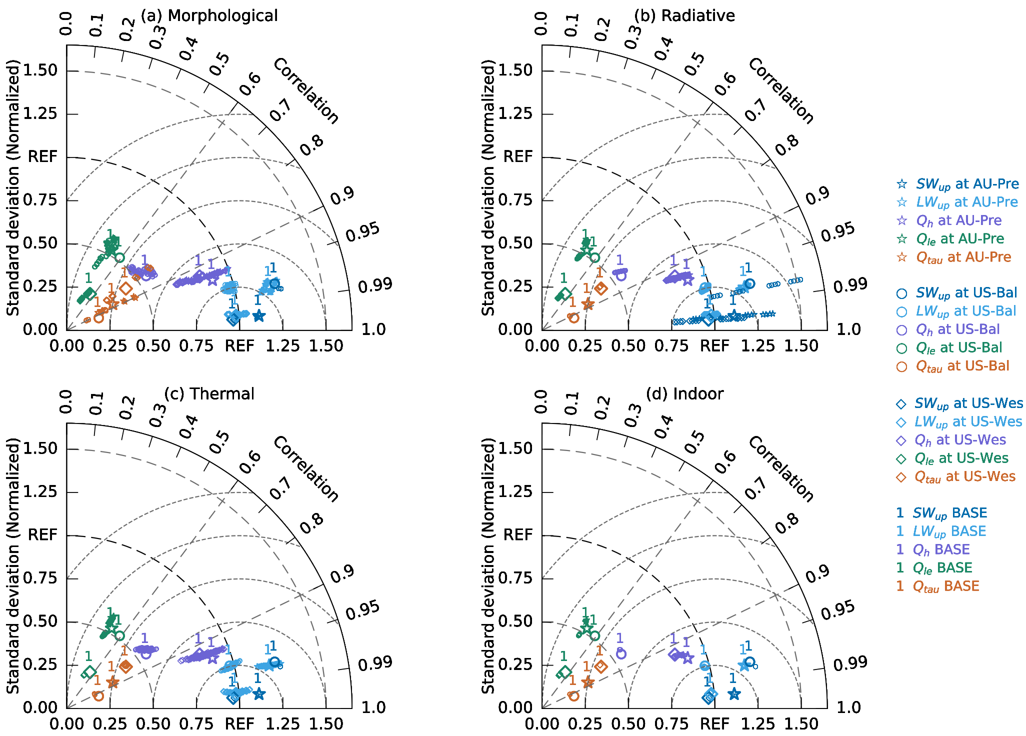

Figure 6. Model sensitivity of half-hourly upward solar radiation (SW_{up}), upward longwave radiation (LW_{up}), sensible heat flux (Q_h), latent heat flux (Q_{le}), and momentum heat flux (Q_{tau}) to parameter uncertainties. The parameter perturbations are grouped into four subsets: (a) morphological parameters, (b) radiative parameters, (c) thermal parameters, and (d) indoor parameters. The BASE simulation serves as the baseline, and the same baseline values are shown in each panel for comparison with the SENS simulation.

SW_{up} was most sensitive to changes in albedo parameters, showing marked variations of σ at all three sites when albedo parameters were perturbed (Figure 6(b)). For instance, at AU-Preston, the σ between modeled and observed SW_{up} in the SENS simulation ranged from 0.9 to 1.3, compared to a baseline value of 1.1. The lowest σ for SW_{up} occurred in the simulation with a 20% reduction in eight albedo parameters, where the decreased albedo also led to the smallest variations in Q_h. Large variations in reflected solar radiation implied changes in its "downstream" variables such as the turbulent fluxes, since albedo directly affected the absorbed energy at the surface. Among the surface albedo parameters, roof albedo had the greatest impact on SW_{up}, followed by wall albedo, impervious road albedo, and pervious road albedo. This could be attributed to findings by Sun et al. (2024), which indicated that roofs were the most efficient urban surfaces for reflecting solar radiation compared to walls and roads in the model. In contrast, SW_{up} was relatively insensitive to variations in morphological, thermal, and indoor parameters, remaining nearly unchanged unless albedo is altered. Emissivity parameters, particularly roof emissivity, primarily affected longwave radiation. Although the variations in LW_{up} due to introducing $\pm$ 2% perturbations to emissivity were small, Oleson, Bonan, Feddema, and Vertenstein (2008) have demonstrated that even minor changes in emissivity can notably affect longwave radiation.

Perturbations in thermal parameters also led to variations in LW_{up} and Q_h, while having rather minimal impact on SW_{up}, Q_{le}, and Q_{tau} (Figure 6(c)). These changes were comparable to the variation patterns caused by morphological parameter perturbations

(Figure 6(a)). At AU-Preston, the σ of Q_h under the thermal parameter perturbations ranged from 0.8 to 0.9, closely resembling the σ of Q_h under morphological parameter perturbations, which ranged from 0.7 to 1.0.

Compared to uncertainties in morphological, radiative, and thermal parameters, those caused by variations in T_BUILDING_MIN were relatively minor (Figure 6(d)). According to Figure 7(a)–(c), the largest difference in anthropogenic heat flux (ΔQ_{ahf}) between the SENS simulation, where T_BUILDING_MIN was increased by 20%, and the BASE simulation (baseline), reached approximately 6 W m^{-2} across the three sites. These sites, located in different background climate types, displayed various patterns of urban heating use. There was a positive correlation between T_BUILDING_MIN and heat flux. Higher T_BUILDING_MIN required more urban heating, which increased waste heat emission into the urban canyon and subsequently raised the urban sensible heat flux. In a cold climate like US-Baltimore, Q_{ahf} varied from 12.0 W m^{-2} (with a 20% decrease in T_BUILDING_MIN) to 19.3 W m^{-2} (with a 20% increase in T_BUILDING_MIN) (Figure 7(b)), showing a widening gap between modeled Q_{ahf} values. The cold climate required substantial heating to maintain indoor temperature at the threshold, which might lead to the overestimation of anthropogenic heat emissions. However, increasing T_BUILDING_MIN reduced the gap between the modeled and reference Q_h (Figure 7(e)). Comparatively, at AU-Preston, located in a temperate climate, Q_{ahf} varied between 0.3 to 5.5 W m^{-2} (Figure 7(a)). At US-WestPhoenix, in an arid climate, Q_{ahf} ranged from 1.4 to 9.1 W m^{-2} (Figure 7(c)). Increasing T_BUILDING_MIN at these two sites with temperate and arid climates helped address the underestimation of Q_{ahf} but might overestimate Q_h (Figure 7(d) and (f)). In contrast, at US-Baltimore with a cold climate, increasing T_BUILDING_MIN reduced the gap between observed and modeled Q_h, but the values remained underestimated. Therefore, when representing the T_BUILDING_MIN as the threshold for urban heating, it was supposed to account for the background climate of each LCZ class.

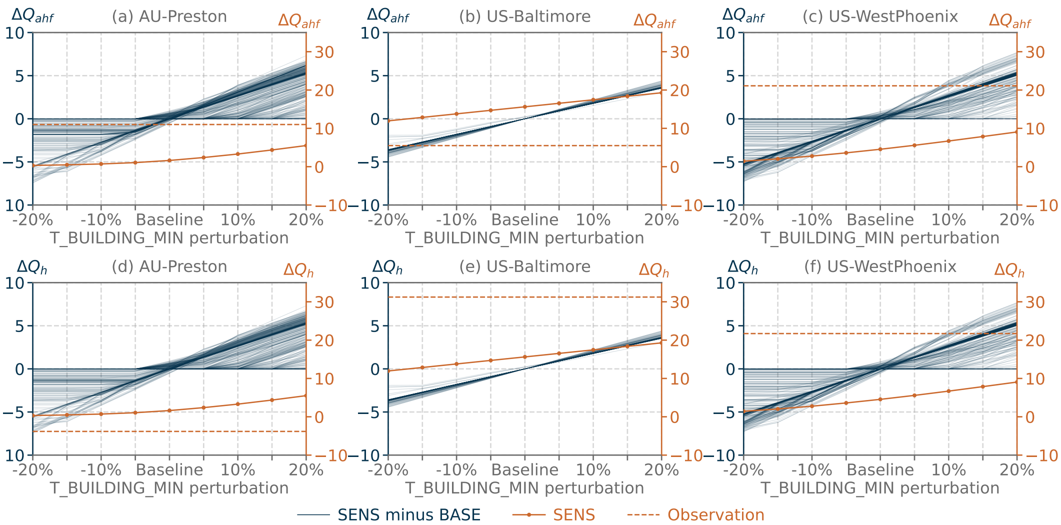

Figure 7. Variations in anthropogenic heat flux (Q_{ahf}) and sensible heat flux (Q_h) due to perturbation in the minimum indoor temperature. (a) and (d) AU-Preston flux tower site, located in a temperate climate zone. (b) and (e) US-Baltimore flux tower site, located in a cold climate zone. (c) and (f) US-WestPhoenix flux tower site, located in an aris climate zone. The left axis denotes the half-hourly difference Δ between the SENS simulation (perturbed by $\pm$ 5%, $\pm$ 10%, $\pm$ 15%, $\pm$ 20%) and the BASE simulation (baseline). The right axis denotes the mean values of fluxes from both simulations and observations.

5 Conclusions and Implications

In this study, we integrated the local climate zone (LCZ) approach within the Community Earth System Model (CESM) to better represent urban land cover heterogeneity. This marked the first implementation of the LCZ framework into a global climate model/Earth system model in a modular way. We validated the model functionality and evaluated the model sensitivity to input urban parameters against 20 global urban flux tower sites. For model validation, we conducted single-point simulations and evaluated the model performance using LCZ urban parameter tables. The results showed that model performance with LCZs was highly dependent on the urban parameters used. In terms of site-averaged normalized standard deviation and correlation coefficient, the LCZ approach reproduced more accurate results for simulating upward longwave radiation flux and anthropogenic heat flux compared to using the three-class urban representation, which used the default urban parameter dataset. However, simulations also had more uncertainties in sensible heat flux using thermal parameters from LCZ tables. To better understand the model sensitivity to various urban parameters, we performed a sensitivity experiment by introducing perturbation factors. The model sensitivity tests revealed that the greatest uncertainties arose from surface albedo. Urban solar radiation flux was particularly sensitive to roof albedo. Morphological and thermal parameters affected sensible heat flux and longwave radiation, where canyon height-to-width ratio, roof fraction, volumetric heat capacity of roof, and the thermal capacity of roof played a dominant role. In comparison to the perturbations of morphological, radiative, and thermal parameters, uncertainties due to the minimum indoor temperature had relatively minimal impacts but affected anthropogenic heat flux and sensible heat flux by changing the thermal conditions inside buildings, which in turn influenced the urban canyon environment.

Single-point simulations using built LCZ data offer valuable insights for urban design and planning, particularly in addressing the challenges of global climate change, emphasizing the need for urban climate adaptation and mitigation strategies. The LCZ framework enables a more precise classification of urban areas, thereby enhancing the accuracy of urban climate simulations. Additionally, it ensures consistency in atmospheric forcing and model configuration for cross-LCZ comparisons within a grid cell. This enables the evaluation of key urban climate indicators, such as urban heat island intensity and heat stress, providing urban designers and planners with critical information on how various urban climates manifest across the ten built LCZ classes. Such climatic insights help guide urban planners and government authorities in selecting appropriate LCZ classes and adjustments to their distribution, thereby facilitating more effective urban development, infrastructure planning, and the integration of green spaces.

We acknowledge the limitations of the current LCZ-based urban parameters, as the use of the LCZ urban parameter table is a simplification approach that has primarily been used at regional scales. While the ten urban landunit classes defined by LCZs provide a more detailed representation of urban landunit heterogeneity, this approach, relying on a look-up table, does not capture global spatial variability as effectively as the default dataset. The three-class approach includes urban parameter variations across 33 global regions, offering more localized details. With ESMs/GCMs increasingly advancing forward kilometer-scale (or higher) resolution (Cheng et al., 2024; Lean et al., 2024; L. Li et al., 2024), LCZ urban parameters at finer scales are crucial to reduce uncertainties. The default urban inputs in CLMU explicitly account for construction details at each urban vertical level using the "nlevurb" dimension, whereas the current LCZ urban parameter tables simplify prescribed thermal properties by assuming averaged values across these levels. The minimum indoor temperature, also prescribed without spatial variability, does not account for dependence on the background climate, limiting its accuracy. Our study focuses on understanding model sensitivity to urban parameters while leaving the development of global LCZ urban parameter datasets for future research. We recommend prioritizing improvements to datasets on morphological characteristics, as well as roof radiative and thermal properties. Users are encouraged to customize LCZ urban parameters within the CESM-compatible surface data. Furthermore, we also acknowledge that our simulations are based on static land surface data while resolving changes in urban land cover could be realized in the next generation of CESM (Fang et al., 2023), with future efforts of interannual LCZ maps (Qi et al., 2024). Therefore, more complex LCZ urban datasets on a global scale with location-specific parameters and transient land cover are needed to improve modeling accuracy and reliability for global climate models (Figure C1).

Appendix A Inputs for single-point simulations

A1 Urban-PLUMBER flux tower sites

The Urban-PLUMBER project (M. J. Lipson et al., 2023) aimed at assessing the performance of thirty urban models through simulations at urban flux tower sites worldwide (Figure A1). These sites have different background climates including tropical, arid, temperate, and cold climates.

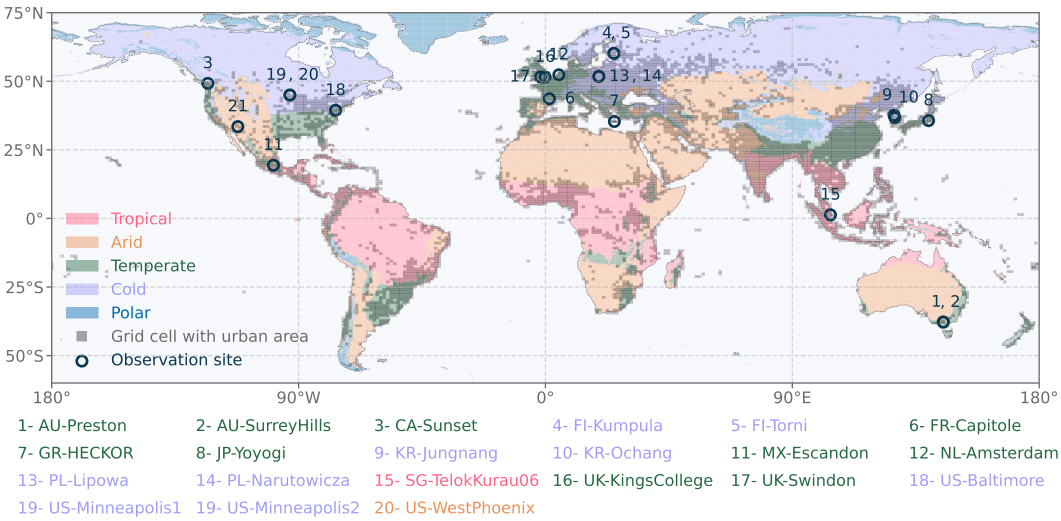

Figure A1. 20 observation sites (21 dots in total) for single-point model validation. Each hollow circle denotes the location of a heat flux tower site in the Urban-PLUMBER project. Observation data from the US-Minneapolis site are divided into US-Minneapolis1 (vegetated areas with few built structures) and US-Minneapolis2 (residential areas). The climate classification comes from a Köppen-Geiger map developed by Beck et al. (2023). Grid cells with urban areas are based on Jackson et al. (2010).

A2 LCZ classes over Urban-PLUMBER sites

Table A1 lists the percentage of urban fractions based on the LCZ classification for Urban-PLUMBER heat flux sites. We used the Google Earth Engine platform (`https://developers.google.com/earth-engine/datasets/catalog/RUB_RUBCLIM_LCZ_global_lcz_map_latest`) (Demuzere, Kittner, et al., 2022) to map the percentage of LCZ fractions within the site domain of a 500 m radius. This domain scale was decided based on the footprint of local urban parameters (M. J. Lipson et al., 2023). We excluded natural land cover, classified as LCZ A–F, from simulations to focus on urban modeling.

Table A1. Percentage of urban landunit fraction for each LCZ class.

No.	Flux tower site name	City	Country	Climate	Percentage of urban landunit classes (%)									
					LCZ1	LCZ2	LCZ3	LCZ4	LCZ5	LCZ6	LCZ7	LCZ8	LCZ9	LCZ10
1	AU-Preston	Melbourne	Australia	Temperate	0	0	0	0	0	100	0	0	0	0
2	AU-SurreyHills	Melbourne	Australia	Temperate	0	0	0	0	0	100	0	0	0	0
3	CA-Sunset	Vancouver	Canada	Temperate	0	0	0	0	0	100	0	0	0	0
4	FI-Kumpula	Helsinki	Finland	Cold	0	0	0	7.2	57.4	5.6	0	29.8	0	0
5	FI-Torni	Helsinki	Finland	Cold	68.7	28.0	0	0	0	0	0	0	0	3.3
6	FR-Capitole	Toulouse	France	Temperate	0	100	0	0	0	0	0	0	0	0
7	GR-HECKOR	Heraklion	Greece	Temperate	0	0	48.2	0	0	3.0	0	48.8	0	0
8	JP-Yoyogi	Tokyo	Japan	Temperate	0	81.1	0	0	18.9	0	0	0	0	0
9	KR-Jungnang	Seoul	South Korea	Cold	0	100	0	0	0	0	0	0	0	0
10	KR-Ochang	Ochang	South Korea	Cold	0	0	0	0	0	0	0	99.4	0	0.6
11	MX-Escandon	Mexico City	Mexico	Temperate	0	14.9	83.9	0	1.2	0	0	0	0	0
12	NL-Amsterdam	Amsterdam	Netherlands	Temperate	0	86.7	0	11.0	2.3	0	0	0	0	0
13	PL-Lipowa	Łódź	Poland	Cold	0	0.5	0	9.5	90.0	0	0	0	0	0
14	PL-Narutowicza	Łódź	Poland	Cold	0	0	0	0	97.2	0	0	2.8	0	0
15	SG-TelokKurau06	Singapore	Singapore	Tropical	0	2.8	97.2	0	0	0	0	0	0	0
16	UK-KingsCollege	London	UK	Temperate	6.3	77.0	0	16.1	0	0	0	0	0	0.6
17	UK-Swindon	Swindon	UK	Temperate	0	0	0	0	0	100	0	0	0	0
18	US-Baltimore	Baltimore	USA	Cold	0	0	0	0	0	100	0	0	0	0
19	US-Minneapolis1	Minneapolis	USA	Cold	0	0	0	0	0	100	0	0	0	0
	US-Minneapolis2	Minneapolis	USA	Cold	0	0	0	0	0	100	0	0	0	0
20	US-WestPhoenix	Phoenix	USA	Arid	0	0	0	0	0	99.9	0	0.1	0	0

A3 LCZ urban parameters

Table A2 lists the parameters from WRF's LCZ urban parameter table (`https://github.com/wrf-model/WRF/blob/master/run/URBPARM_LCZ.TBL`) in updated WRF4.6.0, and C. Li et al. (2023)'s LCZ urban parameter table for CLM5, used for WRF_LCZ and LI_LCZ simulations, respectively. WRF's LCZ urban parameter table mainly focuses on morphological classification, assuming the same radiative and thermal properties over LCZ classes.

Table A2. Comparisons of two existing LCZ urban parameter tables.

Attribute	Urban parameter name	Table name	LCZ1	LCZ2	LCZ3	LCZ4	LCZ5	LCZ6	LCZ7	LCZ8	LCZ9	LCZ10
Morphological parameters	CANYON_HWR!	WRF's	1.88	1.25	1.25	0.75	0.50	0.50	0.90	0.20	0.15	0.35
		LI's	2.50	1.25	1.25	1.00	0.50	0.50	1.50	0.20	0.15	0.35
		Ratio	0.75	1	1	0.75	1	1	0.60	1	1	1
	HT_ROOF!	WRF's	37.50	17.50	6.50	37.50	17.50	6.50	3.00	6.50	6.50	10.00
		LI's	37.50	17.50	6.50	30.00	17.50	6.50	3.00	6.50	6.50	10.00
		Ratio	1	1	1	1.25	1	1	1	1	1	1
	NLEV_IMPROAD	WRF's					-					
		LI's					-					
	THICK_WALL	WRF's					0.20					
		LI's	0.30	0.25	0.25	0.20	0.20	0.20	0.10	0.20	0.20	0.05
		Ratio	0.67	0.80	0.80	1	1	1	2	1	1	4
	THICK_ROOF	WRF's					0.20					
		LI's	0.30	0.30	0.20	0.30	0.25	0.15	0.10	0.12	0.15	0.05
		Ratio	0.67	0.67	1	0.67	0.80	1.33	2	1.67	1.33	4
	WTLUNIT_ROOF!	WRF's	0.53	0.61	0.65	0.46	0.43	0.50	0.88	0.47	0.50	0.45
		LI's	0.50	0.50	0.55	0.30	0.30	0.30	0.75	0.40	0.15	0.25
		Ratio	1.05	1.22	1.18	1.54	1.43	1.67	1.18	1.18	3.33	1.82
	WTROAD_PERV!	WRF's					-					
		LI's	0.10	0.20	0.33	0.50	0.43	0.43	0.60	0.25	0.82	0.60
Radiative parameters	ALB_IMPROAD_DIF*, ALB_IMPROAD_DIR*	WRF's					0.08					
		LI's	0.14	0.14	0.14	0.14	0.14	0.14	0.18	0.14	0.14	0.14
		Ratio	0.57	0.57	0.57	0.57	0.57	0.57	0.44	0.57	0.57	0.57
	ALB_PERROAD_DIF*, ALB_PERROAD_DIR*	WRF's					-					
		LI's					0.22					
	ALB_ROOF_DIF*, ALB_ROOF_DIR*	WRF's					0.30					
		LI's	0.23	0.28	0.25	0.23	0.23	0.23	0.55	0.28	0.23	0.20
		Ratio	1.30	1.07	1.20	1.30	1.30	1.30	0.55	1.07	1.30	1.50
	ALB_WALL_DIF*, ALB_WALL_DIR*	WRF's					0.30					
		LI's	0.35	0.30	0.30	0.35	0.35	0.35	0.55	0.35	0.35	0.30
		Ratio	0.86	1	1	0.86	0.86	0.86	0.55	0.86	0.86	1
	EM_IMPROAD	WRF's					0.95					
		LI's	0.91	0.91	0.91	0.91	0.91	0.91	0.88	0.91	0.91	0.91
		Ratio	1.04	1.04	1.04	1.04	1.04	1.04	1.08	1.04	1.04	1.04
	EM_PERROAD	WRF's					-					
		LI's					0.95					
	EM_ROOF	WRF's					0.90					
		LI's	0.91	0.91	0.91	0.91	0.91	0.91	0.88	0.91	0.91	0.91
		Ratio	0.99	0.99	0.99	0.99	0.99	0.99	1.02	0.99	0.99	0.99
	EM_WALL	WRF's					0.90					
		LI's					0.90					
		Ratio					1					
Thermal parameters	CV_IMPROAD	WRF's					1.74					
		LI's					1.85					
		Ratio					0.94					
	CV_ROOF	WRF's					1.32					
		LI's	1.32	1.32	1.32	1.80	1.32	1.32	2.00	2.11	1.32	2.00
		Ratio	1	1	1	0.73	1	1	0.66	0.63	1	0.66
	CV_WALL	WRF's					1.54					
		LI's	1.54	1.54	1.54	2.00	1.54	1.54	2.00	2.11	1.54	1.59
		Ratio	1	1	1	0.77	1	1	0.77	0.73	1	0.97
	TK_IMPROAD	WRF's					0.82					
		LI's					0.78					
		Ratio					1.05					
	TK_ROOF	WRF's					1.54					
		LI's	1.70	1.70	1.09	1.25	1.70	1.09	0.50	1.07	1.09	2.00
		Ratio	0.91	0.91	1.41	1.23	0.91	1.41	3.18	1.44	1.41	0.77
	TK_WALL	WRF's					1.51					
		LI's	1.27	2.60	1.66	1.45	1.88	1.66	0.18	1.07	1.66	1.42
		Ratio	1.19	0.58	0.91	1.04	0.8	0.91	8.39	1.41	0.91	1.06
Indoor parameters	T_BUILDING_MIN	WRF's					-					
		LI's					283.15					
	T_BUILDING_MAX	WRF's					-					
		LI's					298.15					

1 - denotes no parameters provided for pervious surfaces and indoor temperature in WRF.

2 Parameters labeled with ! and * in three single-point simulations were provided by the Urban-PLUMBER project. In CNTL, WRF_LCZ, LI_LCZ, and CESM_LCZ simulations, albedo parameters (labeled with *) come from an averaged albedo value as provided at each site.

3 Ratio denotes WRF's to LI's ratio.

We refined the urban parameters from two existing LCZ urban parameter tables to develop a new LCZ urban parameter table. Our approach primarily used parameters from LI's LCZ tables, with exceptions for specific parameters where alternative data sources were more similar to the default data. Specifically, we adopted values for CANYON_HWR, HT_ROOF, and WTLUNIT_ROOF from WRF's LCZ table, as they were more closely aligned with the default parameters. We modified ALB_PERROAD_*, where LI's LCZ table set a value of 0.22, which was rather higher compared to the default value of 0.08. Therefore, we set ALB_PERROAD_* to 0.08 in our newly developed LCZ urban parameter table. Similarly, we adjusted ALB_WALL_* from LI's tables by reducing it by 0.05.

Table A3 compares the newly developed urban parameters for 10 LCZ classes with the default parameters for three classes. A limitation of the current LCZ urban parameters is the lack of global spatial variability, as the parameters are uniformly applied without accounting for regional differences. Additionally, the thermal parameters in the LCZ tables do not reflect detailed construction characteristics, leading to a simplified representation of urban thermal properties.

Table A3. Comparisons of newly developed LCZ urban parameters and default urban parameters in CESM.

Attribute	Urban parameter name	LCZ urban parameters										Default urban parameters		
		LCZ1	LCZ2	LCZ3	LCZ4	LCZ5	LCZ6	LCZ7	LCZ8	LCZ9	LCZ10	TBD	HD	MD
Morphological parameters	CANYON_HWR	2.50	1.25	1.25	0.75	0.50	0.50	0.90	0.20	0.15	0.35	5.05 (2.40–8.00)	1.56 (0.80–1.80)	0.65 (0.32–1.60)
	HT_ROOF	37.50	17.50	6.50	37.50	17.50	6.50	3.00	6.50	6.50	10.00	126.34 (60.00–200.00)	39.02 (20.00–45.00)	13.17 (8.00–17.00)
	NLEV_IMPROAD	3	2	2	3	2	2	2	2	2	2	2, 3	2, 3	2
	THICK_ROOF	0.30	0.30	0.20	0.30	0.25	0.15	0.10	0.12	0.15	0.10	0.25 (0.12–0.26)	0.20 (0.12–0.26)	0.18 (0.12–0.26)
	THICK_WALL	0.30	0.25	0.25	0.20	0.20	0.20	0.10	0.20	0.20	0.10	0.32 (0.20–0.32)	0.30 (0.20–0.32)	0.29 (0.19-0.32)
	WTLUNIT_ROOF	0.53	0.61	0.65	0.46	0.43	0.50	0.88	0.47	0.50	0.45	0.61 (0.40–0.85)	0.61 (0.40–0.80)	0.44 (0.20–0.80)
	WTROAD_PERV	0.10	0.20	0.33	0.50	0.43	0.43	0.60	0.25	0.82	0.60	0.27 (0.12–0.71)	0.42 (0.25–1.00)	0.68 (0.43–1.00)
Radiative parameters	ALB_IMPROAD_DIR, ALB_IMPROAD_DIF	0.14	0.14	0.14	0.14	0.14	0.14	0.14	0.14	0.14	0.14	0.22 (0.13–0.23)	0.16 (0.13–0.72)	0.23 (0.08–0.72)
	ALB_PERROAD_DIR, ALB_PERROAD_DIF	0.08	0.08	0.08	0.08	0.08	0.08	0.08	0.08	0.08	0.08	0.08	0.08	0.08
	ALB_ROOF_DIR, ALB_ROOF_DIF	0.23	0.28	0.25	0.23	0.23	0.23	0.25	0.28	0.23	0.20	0.15 (0.14–0.61)	0.24 (0.14–0.61)	0.24 (0.13–0.61)
	ALB_WALL_DIR, ALB_WALL_DIF	0.30	0.25	0.25	0.30	0.30	0.30	0.35	0.30	0.30	0.25	0.22 (0.22–0.55)	0.25 (0.22–0.55)	0.27 (0.22–0.55)
	EM_IMPROAD	0.91	0.91	0.91	0.91	0.91	0.91	0.88	0.91	0.91	0.91	0.88 (0.88–0.91	0.89 (0.28–0.91)	0.90 (0.80–0.93)
	EM_PERROAD	0.95	0.95	0.95	0.95	0.95	0.95	0.95	0.95	0.95	0.95	0.95	0.95	0.95
	EM_ROOF	0.91	0.91	0.91	0.91	0.91	0.91	0.88	0.91	0.91	0.91	0.89 (0.04–0.91)	0.86 (0.04–0.92)	0.87 (0.04–0.92)
	EM_WALL	0.90	0.90	0.90	0.90	0.90	0.90	0.90	0.90	0.90	0.90	0.90 (0.80–0.91)	0.90 (0.80–0.91)	0.90 (0.80–0.93)
Thermal parameters	CV_IMPROAD	1.80	1.80	1.80	1.80	1.80	1.80	1.80	1.80	1.80	1.80	- (0–2.1)	- (0–2.1)	- (0–2.06)
	CV_ROOF	1.32	1.32	1.32	1.80	1.32	1.32	2.00	2.11	1.32	2.00	- (0–3.74)	- (0–3.74)	- (0–3.74)
	CV_WALL	1.54	1.54	1.54	2.00	1.54	1.54	2.00	2.11	1.54	1.59	- (0.10–2.17)	- (0.10–2.18)	- (0.10–2.18)
	TK_IMPROAD	0.80	0.80	0.80	0.80	0.80	0.80	0.80	0.80	0.80	0.80	- (0–1.90)	- (0–1.90)	- (0–1.67)
	TK_ROOF	1.70	1.70	1.09	1.25	1.70	1.09	1.09	1.07	1.09	2.00	0.65 (0.03–45)	0.82 (0.03–45)	0.68 (0.03–45)
	TK_WALL	1.27	2.60	1.66	1.45	1.88	1.66	1.00	1.07	1.66	1.42	- (0.11–6.03)	- (0.11–12.53)	- (0.11–15.85)
Indoor parameters	T_BUILDING_MAX	A time-varying parameter from a separate input file (Oleson & Feddema, 2020).												
	T_BUILDING_MIN	291	287	287	291	287	287	287	287	287	287	290.96 (290.1–292.1)	286.5 (285.1–292.1)	286.38 (285.1–290.1)

1 Given that default parameters vary over 33 regions, this table lists default parameters by their mean values in each urban class with the range from minimum to maximum.

2 "-" denotes that we did not calculate the mean values for thermal parameters in the default dataset. It is not meaningful to calculate means as thermal parameters are 4-dimensional representing thermal properties for each urban layer.

Appendix B Urban surface energy flux

B1 Sensible heat flux

At most sites, variations in modeling sensible heat flux (Q_h) mainly occurred during the daytime. The differences between maximum and minimum sensible heat flux (ΔQ_h) simulated using default parameters are larger than the values using LCZ urban parameters, except for US-Minneapolis2 (Figure B1(t)) sites. Depending on the site, the simulation with LCZs sometimes compares better to observations and sometimes worse.

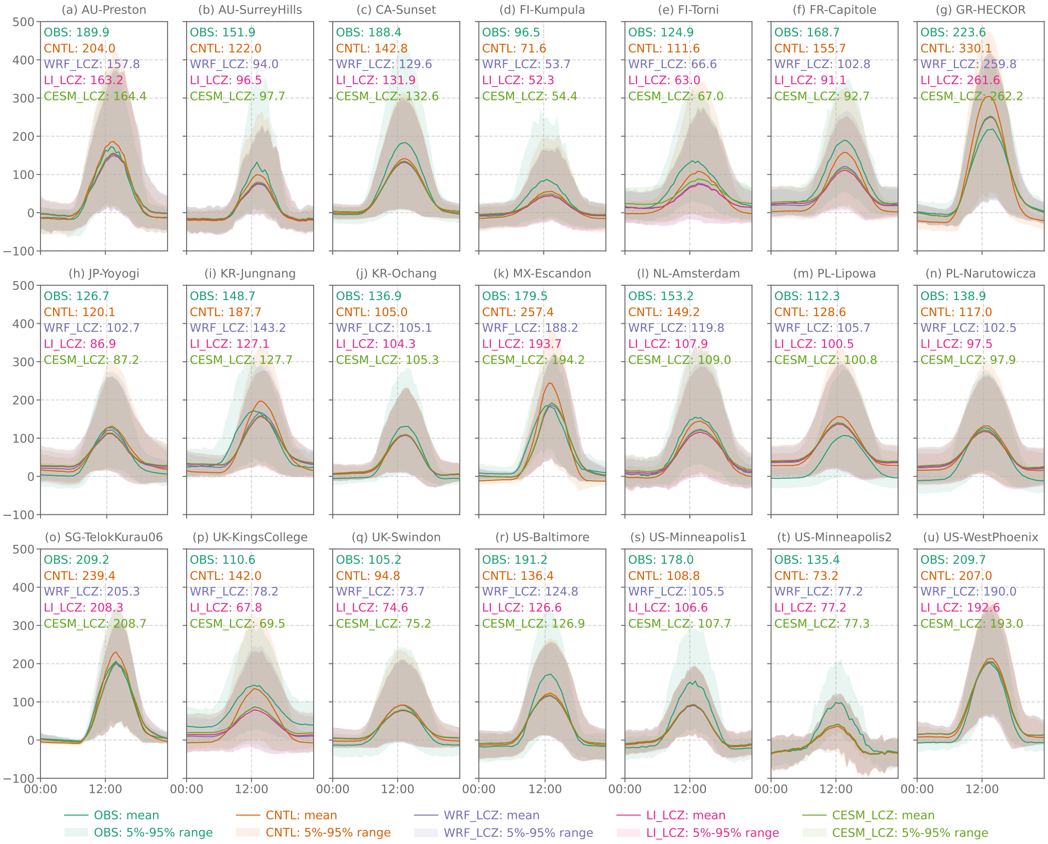

Figure B1. Diurnal variation in sensible heat flux (Q_h, unit: W m^{-2}) over flux tower sites. Texts in each subplot show the averaged differences between maximum and minimum Q_h within a day based on half-hourly values from the observations (OBS), CNTL, WRF_LCZ, LI_LCZ, and CESM_LCZ simulations.

B2 Impacts of roughness length on momentum flux

CLMU generally underestimated the momentum flux (Q_{tau}) over 20 sites, where Q_{tau} was influenced by roughness length (z_0). The CLMU adopted Macdonald et al. (1998)'s empirical method, involving three morphological parameters including roof fraction, building height (H), and canyon height-to-width ratio (hwr). The displacement height (z_d) in the model is calculated as:

$$z_d = (1 + A^{-\lambda_p} \cdot (\lambda_p - 1)) \cdot H, \tag{B1}$$

where A is a constant parameter with a value of 4.43, and λ_p is the plan area density of obstacles. z_0 is calculated as:

$$z_0 = H \cdot \left(1 - \frac{z_d}{H}\right) \cdot \exp\left[-(0.5 \cdot \frac{B \cdot C_d}{K^2} \cdot \left(1 - \frac{z_d}{H}\right) \cdot \lambda_f\right)^{-0.5}\right], \tag{B2}$$

where B is a constant parameter with a value of 1, C_d is a constant parameter with a value of 1.2, and K is the von Karman constant of 0.4. λ_f is the frontal area density of obstacles. The standard code calculates λ_p as:

$$\lambda_p = \frac{hwr}{hwr + 1}, \tag{B3}$$

and λ_f as:

$$\lambda_f = (1 - \lambda_p) \cdot hwr. \tag{B4}$$

We modified the code of calculating z_0 and z_d to keep consistent with the Macdonald et al. (1998)'s method adopted in Urban-PLUMBER project, assuming λ_p equal to the roof fraction (WTLUNIT_ROOF), as:

$$\lambda_p = \text{WTLUNIT\_ROOF}, \tag{B5}$$

and λ_f as:

$$\lambda_f = \frac{wpa}{rpi}. \tag{B6}$$

where *wpa* is wall to plan area ratio, and *rpi* is π.

To test model sensitivity to roughness length and see its impacts on simulating momentum flux and sensible heat flux, we conducted two experiments, one using different equations of calculating z_0, and the other perturbing morphological parameters.

The first experiment had four simulations using corresponding assumption of z_d and z_0, including Urban-PLUMBER's method (CNTL), CLMU's default method (S1), Kanda et al. (2013)'s method (S2), and Kent et al. (2017)'s methods (S3) (Table B1). z_0 was highest in the S2 simulation using Kent et al. (2017)'s method but did not pass the model check that the height of the roof minus the displacement height must be less than or equal to the roughness length ($z_d + z_0 \leq H$). Q_{tau} in the CNTL simulation was higher than S1 and S3 at UK-KingsCollege on 25 December 2012, when higher Q_{tau} amplified Q_h.

Table B1. Model inputs and outputs at UK-KingsCollege.

Simulation name	Inputs				Outputs	
	Reference	Displacement height (z_d, unit: meter)	Roughness length (z_0, unit: meter)	$\frac{z_d}{z_0}$ (unitless)	Momentum flux (Q_{tau}, unit: W m^{-2})	Sensible heat flux (Q_h, unit: W m^{-2})
CNTL	Macdonald et al. (1998)	14.25	1.79	7.96	0.28	−8.91
S1	Macdonald et al. (1998)	16.75	0.98	17.63	0.20	−7.45
S2	Kanda et al. (2013)	27.62	2.53	10.92	No simulation output as the sum of z_d and z_0 over H of 21.3 m	
S3	Kent et al. (2017)	14.65	1.68	8.72	0.27	−8.72

1 Both CNTL and S1 simulations used the Macdonald et al. (1998)'s method of calculating z_d and z_0 but with different assumption of λ_p and λ_f.

2 The CNTL simulation calculated λ_p and λ_f using the Equation B5 and Equation B6 while S1 simulation using Equation B3 and Equation B4.

3 Outputs were calculated as mean values on 25 December 2012.

Another model sensitivity experiment by introducing perturbation factors of +20% and −20% to roof fraction and building height in the SENS simulation (Table B2). It examined Q_{tau} sensitivity to morphological parameters under the same assumption of calculating z_d and z_0 as the Urban-PLUMBER's way based on Macdonald et al. (1998).

811 The modeled Q_{tau} was sensitive to roughness length, while the sensitivity varied over
812 sites (Figure B2).

Table B2. Model inputs and outputs at the AU-Preston, US-Baltimore, and US-WestPhoenix flux tower sites.

Flux tower site name	Simulation name	Inputs					Outputs
		Roof fraction (WTLUNIT_ROOF, unit: %)	Building height (H, unit: m)	Displacement height (z_d, unit: m)	Roughness length (z_0, unit: m)	$\frac{z_d}{z_0}$ (unitless)	Momentum flux (Q_{tau}, unit: W m^{-2})
AU-Preston	BASE	50	6.5	4.96	0.08	62.00	0.10
	SENS1	60	7.8	6.52	0.04	163.00	0.07
	SENS2	60	5.2	4.35	0.02	217.50	0.07
	SENS3	40	7.8	5.22	0.21	24.86	0.14
	SENS4	40	5.2	3.48	0.14	24.86	0.12
US-Baltimore	BASE	50	6.5	4.96	0.02	248.00	0.07
	SENS1	60	7.8	6.52	0.01	652.00	0.05
	SENS2	60	5.2	4.35	0.00	–	0.05
	SENS3	40	7.8	5.22	0.06	87.00	0.09
	SENS4	40	5.2	3.48	0.04	87.00	0.08
US-WestPhoenix	BASE	50	6.5	4.96	0.13	38.15	0.03
	SENS1	60	7.8	6.52	0.07	93.14	0.02
	SENS2	60	5.2	4.35	0.04	108.75	0.02
	SENS3	40	7.8	5.22	0.32	16.31	0.04
	SENS4	40	5.2	3.48	0.22	15.82	0.03

1 All simulations calculated λ_p and λ_f using the Equation B5 and Equation B6.

2 The momentum flux was calculated as the mean values over a seven-day simulation period for analysis.

3 Compared to the parameters in the BASE simulation, roof fraction was perturbed by +20%, +20%, −20%, and −20%, in the SENS1, SENS2, SENS3, and SENS4, respectively. Building height was perturbed by +20%, −20%, +20%, and −20% in the SENS1, SENS2, SENS3, and SENS4 simulations, respectively.

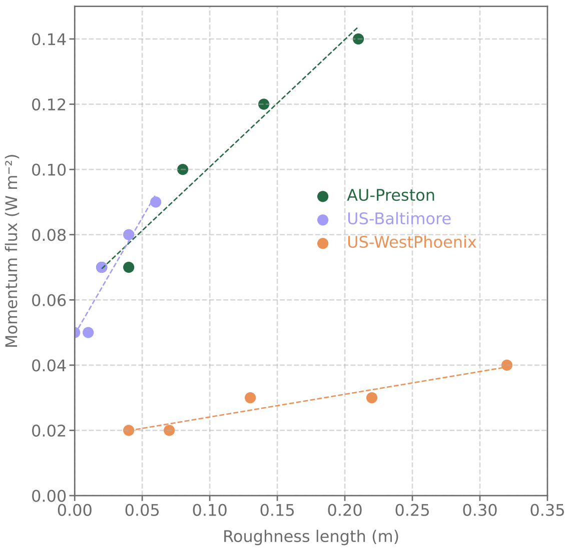

Figure B2. Momentum flux sensitivity to roughness length.

Appendix C Future direction

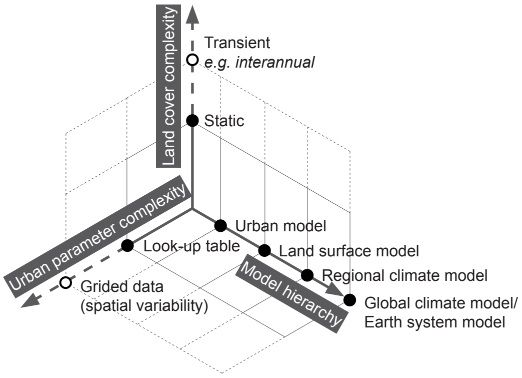

Figure C1. Simulating urban climate with LCZs.

Open Research

Community Earth System Model (CESM) source code is open access: `https://github.com/ESCOMP/CESM`. Community Land Model (CLM) source code is available at: `https://github.com/ESCOMP/CTSM`. Observation data from the Urban-PLUMBER project is available at: `https://zenodo.org/records/7104984`. The global 100 m LCZ map is available at: `https://zenodo.org/records/8419340`. The default input data participating in the Urban-PLUMBER was generated by Dr. Keith W. Oleson using the "mksurfdata_map" tool in the CLM with the version tag "release-clm5.0.34". The modified code with modularized built LCZ representation, as well as land surface inputs with LCZ urban parameters over Urban-PLUMBER sites, and other supplementary materials, are available in the author's GitHub repository: `https://github.com/envdes/code_CESM_LCZ` (Sun & Zheng, 2025).

Acknowledgments

We dedicate this work to the memory of Dr. Jason Ching, whose groundbreaking contributions and inspiring vision laid the foundation for this research. His legacy continues to guide and inspire us. This work used the ARCHER2 UK National Supercomputing Service (`https://www.archer2.ac.uk`) and JASMIN, the UK's collaborative data analysis environment (`https://www.jasmin.ac.uk`). This work was supported by the U.K. Natural Environment Research Council. The authors would like to acknowledge the assistance of Research IT and the use of the HPC Pool and Computational Shared Facility at The University of Manchester. The support of Dr. Douglas Lowe and Christopher Grave from Research IT at The University of Manchester is gratefully acknowledged. We thank Prof. David M. Schultz for his comments on an earlier version of the manuscript. Additionally, we appreciate the assistance of Dr. Congyuan Li at the National University of Defense Technology in China. Z.Z. appreciates the support provided by the academic start-up funds from the Department of Earth and Environmental Sciences at The University of Manchester. Y.S. is supported by Z.Z's academic start-up funds. Contributions from K.W.O. are based upon work supported by the NSF National Center for Atmospheric Research, which is a major facility sponsored by the U.S. National Science Foundation under Cooperative Agreement No. 1852977. Contributions from M.D. are supported by the European Union's HORIZON Research and Innovation Actions under grant agreement No. 101137851, project CARMINE (Climate-Resilient Development Pathways in Metropolitan Regions of Europe, `https://www.carmine-project.eu/`). L.Z.

acknowledges the support of the U.S. National Science Foundation (CAREER award grant no. 2145362). The authors declare no conflict of interest.

References

Akbari, H., Matthews, H. D., & Seto, D. (2012). The long-term effect of increasing the albedo of urban areas. *Environmental Research Letters*, *7*(2), 024004. doi: 10.1088/1748-9326/7/2/024004

Alexander, P., Bechtel, B., Chow, W., Fealy, R., Mills, G., Kwok, Y. T., ... Ng, E. (2016). Linking urban climate classification with an urban energy and water budget model: Multi-site and multi-seasonal evaluation. *Urban Climate*, *17*, 196–215. doi: 10.1016/j.uclim.2016.08.003

Alexander, P. J., Mills, G., & Fealy, R. (2015). Using LCZ data to run an urban energy balance model. *Urban Climate*, *13*, 14–37. doi: 10.1016/j.uclim.2015.05.001

Artis, D. A., & Carnahan, W. H. (1982). Survey of emissivity variability in thermography of urban areas. *Remote Sensing of Environment*, *12*(4), 313–329. doi: 10.1016/0034-4257(82)90043-8

Aslam, A., & Rana, I. A. (2022). The use of local climate zones in the urban environment: A systematic review of data sources, methods, and themes. *Urban Climate*, *42*, 101120. doi: 10.1016/j.uclim.2022.101120

Beck, H. E., McVicar, T. R., Vergopolan, N., Berg, A., Lutsko, N. J., Dufour, A., ... Miralles, D. G. (2023). High-resolution (1 km) Köppen-Geiger maps for 1901–2099 based on constrained CMIP6 projections. *Scientific Data*, *10*(1), 724. doi: 10.1038/s41597-023-02549-6

Best, M. J., & Grimmond, C. S. B. (2016). Investigation of the impact of anthropogenic heat flux within an urban land surface model and PILPS-urban. *Theoretical and Applied Climatology*, *126*(1), 51–60. doi: 10.1007/s00704-015-1554-3

Best, M. J., Pryor, M., Clark, D. B., Rooney, G. G., Essery, R. L. H., Ménard, C. B., ... Harding, R. J. (2011). The Joint UK Land Environment Simulator (JULES), model description – Part 1: Energy and water fluxes. *Geoscientific Model Development*, *4*(3), 677–699. doi: 10.5194/gmd-4-677-2011

Brousse, O., Martilli, A., Foley, M., Mills, G., & Bechtel, B. (2016). WUDAPT, an efficient land use producing data tool for mesoscale models? Integration of urban LCZ in WRF over Madrid. *Urban Climate*, *17*, 116–134. doi: 10.1016/j.uclim.2016.04.001

Brousse, O., Wouters, H., Demuzere, M., Thiery, W., Van de Walle, J., & van Lipzig, N. P. M. (2020). The local climate impact of an African city during clear-sky conditions—Implications of the recent urbanization in Kampala (Uganda). *International Journal of Climatology*, *40*(10), 4586–4608. doi: 10.1002/joc.6477

Caluwaerts, S., Hamdi, R., Top, S., Lauwaet, D., Berckmans, J., Degrauwe, D., ... Termonia, P. (2020). The urban climate of Ghent, Belgium: A case study combining a high-accuracy monitoring network with numerical simulations. *Urban Climate*, *31*, 100565. doi: 10.1016/j.uclim.2019.100565

Cheng, Y., Zhao, L., Chakraborty, T., Oleson, K., Demuzere, M., Liu, X., ... Li, X. (2024). U-Surf: A Global 1 km spatially continuous urban surface property dataset for kilometer-scale urban-resolving Earth system modeling. *Earth System Science Data Discussions*, 1–38. doi: 10.5194/essd-2024-416

Ching, J., Mills, G., Bechtel, B., See, L., Feddema, J., Wang, X., ... Theeuwes, N. (2018). WUDAPT: An Urban Weather, Climate, and Environmental Modeling Infrastructure for the Anthropocene. *Bulletin of the American Meteorological Society*, *99*(9), 1907–1924. doi: 10.1175/BAMS-D-16-0236.1

Cui, F., Hamdi, R., Kuang, W., Yang, T., He, H., Termonia, P., & De Maeyer,

P. (2023). Interactions between the summer urban heat islands and heat waves in Beijing during 2000–2018. *Atmospheric Research*, *291*, 106813. doi: 10.1016/j.atmosres.2023.106813

Cui, F., Hamdi, R., Yang, T., Termonia, P., & De Maeyer, P. (2024). The summer warming of Beijing (China) under the Paris Agreement. *Theoretical and Applied Climatology*, *155*(9), 8951–8969. doi: 10.1007/s00704-024-05164-6

Danabasoglu, G., Lamarque, J.-F., Bacmeister, J., Bailey, D. A., DuVivier, A. K., Edwards, J., . . . Strand, W. G. (2020). The Community Earth System Model version 2 (CESM2). *Journal of Advances in Modeling Earth Systems*, *12*(2), e2019MS001916. doi: 10.1029/2019MS001916

Demuzere, M., Argüeso, D., Zonato, A., & Kittner, J. (2022). W2W: A Python package that injects WUDAPT's Local Climate Zone information in WRF. *Journal of Open Source Software*, *7*(76), 4432. doi: 10.21105/joss.04432

Demuzere, M., Bechtel, B., Middel, A., & Mills, G. (2019). Mapping Europe into local climate zones. *PLOS ONE*, *14*(4), e0214474. doi: 10.1371/journal.pone.0214474

Demuzere, M., Harshan, S., Järvi, L., Roth, M., Grimmond, C. S. B., Masson, V., . . . Wouters, H. (2017). Impact of urban canopy models and external parameters on the modelled urban energy balance in a tropical city. *Quarterly Journal of the Royal Meteorological Society*, *143*(704), 1581–1596. doi: 10.1002/qj.3028

Demuzere, M., Kittner, J., Martilli, A., Mills, G., Moede, C., Stewart, I. D., . . . Bechtel, B. (2022). A global map of local climate zones to support earth system modelling and urban-scale environmental science. *Earth System Science Data*, *14*(8), 3835–3873. doi: 10.5194/essd-14-3835-2022

Demuzere, M., Oleson, K., Coutts, A. M., Pigeon, G., & van Lipzig, N. P. M. (2013). Simulating the surface energy balance over two contrasting urban environments using the Community Land Model Urban. *International Journal of Climatology*, *33*(15), 3182–3205. doi: 10.1002/joc.3656

Dobson, J., Bright, E., Coleman, P., Durfee, R., & Worley, B. (2000). LandScan: A global population database for estimating populations at risk. *Photogrammetric Engineering and Remote Sensing*, *66*, 849–857.

Dong, Y., Varquez, A. C. G., & Kanda, M. (2017). Global anthropogenic heat flux database with high spatial resolution. *Scientific Data*, *150*, 276–294. doi: 10.1016/j.atmosenv.2016.11.040

Du, R., Liu, C.-H., Li, X.-X., & Lin, C.-Y. (2023). Effect of local climate zone (LCZ) and building category (BC) classification on the simulation of urban climate and air-conditioning load in Hong Kong. *Energy*, *271*, 127004. doi: 10.1016/j.energy.2023.127004

Fang, B., Zhao, L., Oleson, K. W., Zhang, K., Lawrence, P. J., Sacks, B., . . . Lee, X. (2023). *Representing dynamic urban land change in the Community Earth System Model (CESM)* (Tech. Rep.). Preprints. doi: 10.22541/essoar.168676909.95382628/v1

Fernández, M. E., Picone, N., Gentili, J. O., & Campo, A. M. (2021). Analysis of the Urban Energy Balance in Bahía Blanca (Argentina). *Journal of Geophysical Research: Atmospheres*, *37*, 100856. doi: 10.1016/j.uclim.2021.100856

Fletcher, T. D., Andrieu, H., & Hamel, P. (2013). Understanding, management and modelling of urban hydrology and its consequences for receiving waters: A state of the art. *Advances in Water Resources*, *51*, 261–279. doi: 10.1016/j.advwatres.2012.09.001

Geletič, J., Lehnert, M., Dobrovolný, P., & Žuvela-Aloise, M. (2019). Spatial modelling of summer climate indices based on local climate zones: Expected changes in the future climate of Brno, Czech Republic. *Climatic Change*, *152*(3), 487–502. doi: 10.1007/s10584-018-2353-5

Geletič, J., Lehnert, M., Savić, S., & Milošević, D. (2018). Modelled spatiotemporal variability of outdoor thermal comfort in local climate zones of the city of Brno, Czech Republic. *Science of The Total Environment*, *624*, 385–395. doi: 10.1016/j.scitotenv.2017.12.076

Gilabert, J., Deluca, A., Lauwaet, D., Ballester, J., Corbera, J., & Llasat, M. C. (2021). Assessing heat exposure to extreme temperatures in urban areas using the Local Climate Zone classification. *Natural Hazards and Earth System Sciences*, *21*(1), 375–391. doi: 10.5194/nhess-21-375-2021

Gray, L. C., Zhao, L., & Stillwell, A. S. (2023). Impacts of climate change on global total and urban runoff. *Journal of Hydrology*, *620*, 129352. doi: 10.1016/j.jhydrol.2023.129352

Hammerberg, K., Brousse, O., Martilli, A., & Mahdavi, A. (2018). Implications of employing detailed urban canopy parameters for mesoscale climate modelling: A comparison between WUDAPT and GIS databases over Vienna, Austria. *International Journal of Climatology*, *38*(S1), e1241-e1257. doi: 10.1002/joc.5447

Hansen, G., & Stone, D. (2016). Assessing the observed impact of anthropogenic climate change. *Nature Climate Change*, *6*(5), 532–537. doi: 10.1038/nclimate2896

He, X., Li, Y., Wang, X., Chen, L., Yu, B., Zhang, Y., ... Doutriaux, C. (2008). Performance metrics for climate models. *Journal of Geophysical Research: Atmospheres*, *113*(D6). doi: 10.1029/2007JD008972

Hertwig, D., Grimmond, S., Hendry, M. A., Saunders, B., Wang, Z., Jeoffrion, M., ... Kotthaus, S. (2020). Urban signals in high-resolution weather and climate simulations: Role of urban land-surface characterisation. *Theoretical and Applied Climatology*, *142*(1-2), 701–728. doi: 10.1007/s00704-020-03294-1

Hidalgo-García, D., & Rezapouraghdam, H. (2023). Variability of heat stress using the UrbClim climate model in the city of Seville (Spain): Mitigation proposal. *Environmental Monitoring and Assessment*, *195*(10), 1164. doi: 10.1007/s10661-023-11768-8

Huang, F., Jiang, S., Zhan, W., Bechtel, B., Liu, Z., Demuzere, M., ... Chen, J. (2023). Mapping local climate zones for cities: A large review. *Remote Sensing of Environment*, *292*, 113573. doi: 10.1016/j.rse.2023.113573

Hürzeler, A., Hollósi, B., Burger, M., Gubler, M., & Brönnimann, S. (2022). Performance analysis of the urban climate model MUKLIMO_3 for three extreme heatwave events in Bern. *City and Environment Interactions*, *16*, 100090. doi: 10.1016/j.cacint.2022.100090

Jackson, T. L., Feddema, J. J., Oleson, K. W., Bonan, G. B., & Bauer, J. T. (2010). Parameterization of urban characteristics for global climate modelling. *Annals of the Association of American Geographers*, *100*(4), 848–865. doi: 10.1080/00045608.2010.497328

Jin, L., Pan, X., Liu, L., Liu, L., Liu, J., & Gao, Y. (2020). Block-based local climate zone approach to urban climate maps using the UDC model. *Building and Environment*, *186*, 107334. doi: 10.1016/j.buildenv.2020.107334

Kanda, M., Inagaki, A., Miyamoto, T., Gryschka, M., & Raasch, S. (2013). A new aerodynamic parametrization for real urban surfaces. *Boundary-Layer Meteorology*, *148*(2), 357–377. doi: 10.1007/s10546-013-9818-x

Kent, C. W., Grimmond, S., & Gatey, D. (2017). Aerodynamic roughness parameters in cities: Inclusion of vegetation. *Journal of Wind Engineering and Industrial Aerodynamics*, *169*, 168–176. doi: 10.1016/j.jweia.2017.07.016

Kotthaus, S., & Grimmond, C. S. B. (2014). Energy exchange in a dense urban environment – Part II: Impact of spatial heterogeneity of the surface. *Urban Climate*, *10*, 281–307. doi: 10.1016/j.uclim.2013.10.001

Kwok, Y. T., Schoetter, R., de Munck, C., Lau, K. K.-L., Wong, M. S., & Ng, E. (2021). High-resolution mesoscale simulation of the microclimatic effects of urban development in the past, present, and future Hong Kong. *Urban Climate*, *37*, 100850. doi: 10.1016/j.uclim.2021.100850

Kwok, Y. T., Schoetter, R., Lau, K. K.-L., Hidalgo, J., Ren, C., Pigeon, G., & Masson, V. (2019). How well does the local climate zone scheme discern the thermal environment of Toulouse (France)? An analysis using numerical simulation data. *Journal of Geophysical Research: Atmospheres*, *39*(14), 5292–5315. doi: 10.1002/joc.6140

Lawrence, D. M., Fisher, R. A., Koven, C. D., Oleson, K. W., Swenson, S. C., Bonan, G., … Zeng, X. (2019). The Community Land Model version 5: Description of new features, benchmarking, and impact of forcing uncertainty. *Journal of Advances in Modeling Earth Systems*, *11*(12), 4245–4287. doi: 10.1029/2018MS001583

Lean, H. W., Theeuwes, N. E., Baldauf, M., Barkmeijer, J., Bessardon, G., Blunn, L., … Yang, X. (2024). The hectometric modelling challenge: Gaps in the current state of the art and ways forward towards the implementation of 100-m scale weather and climate models. *Quarterly Journal of the Royal Meteorological Society*, *150*(765), 4671 - 4708. doi: 10.1002/qj.4858

Li, C., Zhang, N., Wang, Y., & Chen, Y. (2023). Modeling urban heat islands and thermal comfort during a heat wave event in East China with CLM5 incorporating local climate zones. *Journal of Geophysical Research: Atmospheres*, *128*(16), e2023JD038883. doi: 10.1029/2023JD038883

Li, D., Malyshev, S., & Shevliakova, E. (2016). Exploring historical and future urban climate in the Earth System Modeling framework: 1. Model development and evaluation. *Journal of Advances in Modeling Earth Systems*, *8*(2), 917–935. doi: 10.1002/2015MS000578

Li, L., Bisht, G., Hao, D., & Leung, L. R. (2024). Global 1km land surface parameters for kilometer-scale Earth system modeling. *Earth System Science Data*, *16*(4), 2007–2032. doi: 10.5194/essd-16-2007-2024

Li, L., Zhan, W., Ju, W., Peñuelas, J., Zhu, Z., Peng, S., … Yu, C. (2023). Competition between biogeochemical drivers and land-cover changes determines urban greening or browning. *Remote Sensing of Environment*, *287*, 113481. doi: 10.1016/j.rse.2023.113481

Li, X. C., Zhao, L., Oleson, K., Zhou, Y., Qin, Y., Zhang, K., & Fang, B. (2024). Enhancing urban climate-energy modeling in the Community Earth System Model (CESM) through explicit representation of urban air-conditioning adoption. *Journal of Advances in Modeling Earth Systems*, *16*(4), e2023MS004107. doi: 10.1029/2023MS004107

Li, X. C., Zhao, L., Qin, Y., Oleson, K., & Zhang, Y. (2024). Elevated urban energy risks due to climate-driven biophysical feedbacks. *Nature Climate Change*, *14*(10), 1056–1063. doi: 10.1038/s41558-024-02108-w

Liang, T., He, J., Chen, L., Yao, Z., Zhang, L., Che, H., & Gong, S. (2021). Simulation of the influence of a fine-scale urban underlying surface on the urban heat island effect in Beijing. *Atmospheric Research*, *262*, 105786. doi: 10.1016/j.atmosres.2021.105786

Lipson, M., Grimmond, S., Best, M., Chow, W., Christen, A., Chrysoulakis, N., … Ward, H. C. (2022a). *Data for "Harmonized gap-filled dataset from 20 urban flux tower sites" for the Urban-PLUMBER project.* Zenodo. doi: 10.5281/zenodo.5517550

Lipson, M., Grimmond, S., Best, M., Chow, W. T. L., Christen, A., Chrysoulakis, N., … Wouters, H. (2022b). Harmonized gap-filled datasets from 20 urban flux tower sites. *Earth System Science Data*, *14*(11), 5157–5178. doi: 10.5194/essd-14-5157-2022

Lipson, M., Grimmond, S., Best, M., Christen, A., Coutts, A., Crawford, B., … Kim, Y.-H. (2021). *Urban-PLUMBER: Site information webpage (archive of https://urban-plumber.github.io/sites).* doi: 10.5281/zenodo.4751557

Lipson, M. J., Grimmond, S., Best, M., Abramowitz, G., Coutts, A., Tapper, N.,

... Pitman, A. J. (2023). Evaluation of 30 urban land surface models in the Urban-PLUMBER project: Phase 1 results. *Quarterly Journal of the Royal Meteorological Society*, *n/a*(n/a). doi: 10.1002/qj.4589

Lyu, T., Buccolieri, R., & Gao, Z. (2019). A numerical study on the correlation between sky view factor and summer microclimate of local climate zones. *Atmosphere*, *10*(8), 438. doi: 10.3390/atmos10080438

Macdonald, R. W., Griffiths, R. F., & Hall, D. J. (1998). An improved method for the estimation of surface roughness of obstacle arrays. *Atmospheric Environment*, *32*(11), 1857–1864. doi: 10.1016/S1352-2310(97)00403-2

Maracchini, G., Bavarsad, F. S., Di Giuseppe, E., & D'Orazio, M. (2023). Sensitivity and uncertainty analysis on urban heat island intensity using the local climate zone (LCZ) schema: The case study of Athens. In J. Littlewood, R. J. Howlett, & L. C. Jain (Eds.), *Sustainability in Energy and Buildings 2022* (pp. 281–290). Singapore: Springer Nature. doi: 10.1007/978-981-19-8769-4_27

Masson, V. (2000). A physically-based scheme for the urban energy budget in atmospheric models. *Boundary-Layer Meteorology*, *94*(3), 357–397. doi: 10.1023/A:1002463829265

Meili, N., Acero, J. A., Peleg, N., Manoli, G., Burlando, P., & Fatichi, S. (2021). Vegetation cover and plant-trait effects on outdoor thermal comfort in a tropical city. *Building and Environment*, *195*, 107733. doi: 10.1016/j.buildenv.2021.107733

Middel, A., Häb, K., Brazel, A. J., Martin, C. A., & Guhathakurta, S. (2014). Impact of urban form and design on mid-afternoon microclimate in Phoenix Local Climate Zones. *Landscape and Urban Planning*, *122*, 16–28. doi: 10.1016/j.landurbplan.2013.11.004

Molnár, G., Gyöngyösi, A. Z., & Gál, T. (2019). Integration of an LCZ-based classification into WRF to assess the intra-urban temperature pattern under a heatwave period in Szeged, Hungary. *Theoretical and Applied Climatology*, *138*(1), 1139–1158. doi: 10.1007/s00704-019-02881-1

Moradi, M., Krayenhoff, E. S., & Aliabadi, A. A. (2022). A comprehensive indoor–outdoor urban climate model with hydrology: The Vertical City Weather Generator (VCWG v2.0.0). *Building and Environment*, *207*, 108406. doi: 10.1016/j.buildenv.2021.108406

Moriwaki, R., Kanda, M., Senoo, H., Hagishima, A., & Kinouchi, T. (2008). Anthropogenic water vapor emissions in Tokyo. *Water Resources Research*, *44*(11). doi: 10.1029/2007WR006624

Obe, O. B., Morakinyo, T. E., & Mills, G. (2024). A study of the impact of landscape heterogeneity on surface energy fluxes in a tropical climate using SUEWS. *Scientific Data*, *53*, 101788. doi: 10.1016/j.uclim.2023.101788

Oke, T. R., Mills, G., Christen, A., & Voogt, J. A. (2017). *Urban Climates*. Cambridge University Press.

Oleson, K. W., Bonan, G. B., Feddema, J. J., & Vertenstein, M. (2008). An urban parameterization for a global climate model. Part II: Sensitivity to input parameters and the simulated urban heat island in offline simulations. *Journal of Applied Meteorology and Climatology*, *47*(4), 1061–1076. doi: 10.1175/2007JAMC1598.1

Oleson, K. W., Bonan, G. B., Feddema, J. J., Vertenstein, M., & Grimmond, C. S. B. (2008). An urban parameterization for a global climate model. Part I: Formulation and evaluation for two cities. *Journal of Applied Meteorology and Climatology*, *47*(4), 1038–1060. doi: 10.1175/2007JAMC1597.1

Oleson, K. W., Bonan, G. B., Feddema, J. J., Vertenstein, M., & Kluzek, E. (2010). *Technical description of an urban parameterization for the Community Land Model (CLMU)* (Tech. Rep.). University Corporation for Atmospheric Research.

Oleson, K. W., & Feddema, J. (2020). Parameterization and surface data improvements and new capabilities for the Community Land Model Urban (CLMU). *Journal of Advances in Modeling Earth Systems*, *12*(2), e2018MS001586. doi: 10.1029/2018MS001586

Patel, P., Karmakar, S., Ghosh, S., & Niyogi, D. (2020). Improved simulation of very heavy rainfall events by incorporating WUDAPT urban land use/land cover in WRF. *Urban Climate*, *32*, 100616. doi: 10.1016/j.uclim.2020.100616

Pellegatti Franco, D. M., Andrade, M. d. F., Ynoue, R. Y., & Ching, J. (2019). Effect of Local Climate Zone (LCZ) classification on ozone chemical transport model simulations in Sao Paulo, Brazil. *Urban Climate*, *27*, 293–313. doi: 10.1016/j.uclim.2018.12.007

Qi, M., Xu, C., Zhang, W., Demuzere, M., Hystad, P., Lu, T., … Hankey, S. (2024). Mapping urban form into local climate zones for the continental US from 1986–2020. *Scientific Data*, *11*(1), 195. doi: 10.1038/s41597-024-03042-4

Quah, A. K. L., & Roth, M. (2012). Diurnal and weekly variation of anthropogenic heat emissions in a tropical city, Singapore. *International Journal of Climatology*, *46*, 92–103. doi: 10.1016/j.atmosenv.2011.10.015

Ribeiro, I., Martilli, A., Falls, M., Zonato, A., & Villalba, G. (2021). Highly resolved WRF-BEP/BEM simulations over Barcelona urban area with LCZ. *Atmospheric Research*, *248*, 105220. doi: 10.1016/j.atmosres.2020.105220

Stewart, I. D., & Oke, T. R. (2012). Local climate zones for urban temperature studies. *Bulletin of the American Meteorological Society*, *93*(12), 1879–1900. doi: 10.1175/BAMS-D-11-00019.1

Stewart, I. D., Oke, T. R., & Krayenhoff, E. S. (2014). Evaluation of the 'local climate zone' scheme using temperature observations and model simulations. *International Journal of Climatology*, *34*(4), 1062–1080. doi: 10.1002/joc.3746

Sun, Y., Fang, B., Oleson, K. W., Zhao, L., Topping, D. O., Schultz, D. M., & Zheng, Z. (2024). Improving urban climate adaptation modelling in the Community Earth System Model (CESM) through transient urban surface albedo representation. *Journal of Advances in Modeling Earth Systems*, *16*, e2024MS004380. doi: 10.1029/2024MS004380

Sun, Y., & Zheng, Z. (2025). envdes/code_CESM_LCZ: First Release by envdes (v0.0.0) [Software]. *Zenodo*. doi: 10.5281/zenodo.14883318

Taylor, K. E. (2001). Summarizing multiple aspects of model performance in a single diagram. *Journal of Geophysical Research: Atmospheres*, *106*(D7), 7183–7192. doi: 10.1029/2000JD900719

Tsiringakis, A., Steeneveld, G.-J., Holtslag, A. A. M., Kotthaus, S., & Grimmond, S. (2019). On- and off-line evaluation of the single-layer urban canopy model in London summertime conditions. *Quarterly Journal of the Royal Meteorological Society*, *145*(721), 1474–1489. doi: 10.1002/qj.3505

Unal Cilek, M., & Cilek, A. (2021). Analyses of land surface temperature (LST) variability among local climate zones (LCZs) comparing Landsat-8 and ENVI-met model data. *Sustainable Cities and Society*, *69*, 102877. doi: 10.1016/j.scs.2021.102877

Van de Walle, J., Brousse, O., Arnalsteen, L., Byarugaba, D., Ddumba, D. S., Demuzere, M., … P.M. van Lipzig, N. (2021). Can local fieldwork help to represent intra-urban variability of canopy parameters relevant for tropical African climate studies? *Theoretical and Applied Climatology*, *146*(1), 457–474. doi: 10.1007/s00704-021-03733-7

Varquez, A. C. G., Kiyomoto, S., Khanh, D. N., & Kanda, M. (2017). Global 1-km present and future hourly anthropogenic heat flux. *Scientific Data*, *8*(1), 64. doi: 10.1038/s41597-021-00850-w

Verdonck, M.-L., Demuzere, M., Hooyberghs, H., Beck, C., Cyrys, J., Schneider, A., … Van Coillie, F. (2018). The potential of local climate zones maps as a heat stress assessment tool, supported by simulated air temperature data. *Landscape and Urban Planning*, *178*, 183–197. doi: 10.1016/j.landurbplan.2018.06.004

Ward, H. C., Evans, J. G., & Grimmond, C. S. B. (2016). Multi-season eddy covariance observations of energy, water and carbon fluxes over a suburban area in Swindon, UK. *Journal of Geophysical Research: Atmospheres*, *13*(9), 4645–4666. doi: 10.5194/acp-13-4645-2013

Xu, G., Li, J., Shi, Y., Feng, X., Zhang, Y., Geletič, J., . . . Milošević, D. (2022). Improvements, extensions, and validation of the Urban Weather Generator (UWG) for performance-oriented neighborhood planning. *Urban Climate*, *45*, 101247. doi: 10.1016/j.uclim.2022.101247

Xu, G., Li, J., Shi, Y., Feng, X., Zhang, Y., Geletič, J., . . . Milošević, D. (2023). Simulation of canopy urban heat island at a block scale based on local climate zones and urban weather generator: A case study of Beijing. *International Journal of Remote Sensing*, *45*(19-20), 7160-7184. doi: 10.1080/01431161.2023.2203344

Yang, J., Zhao, L., & Oleson, K. (2023). Large humidity effects on urban heat exposure and cooling challenges under climate change. *Environmental Research Letters*, *18*(4), 044024. doi: 10.1088/1748-9326/acc475

Yin, S., Xiao, S., Ding, X., & Fan, Y. (2024). Improvement of spatial-temporal urban heat island study based on local climate zone framework: A case study of Hangzhou, China. *Building and Environment*, *248*, 111102. doi: 10.1016/j.buildenv.2023.111102

Zhang, H., Bai, J., Zhao, J., Guo, F., Zhu, P., Dong, J., & Cai, J. (2024). Application and future of local climate zone system in urban climate assessment and planning—Bibliometrics and meta-analysis. *Cities*, *150*, 104999. doi: 10.1016/j.cities.2024.104999

Zhang, J., Zhang, K., Liu, J., & Ban-Weiss, G. (2016). Revisiting the climate impacts of cool roofs around the globe using an Earth system model. *Environmental Research Letters*, *11*(8), 084014. doi: 10.1088/1748-9326/11/8/084014

Zhang, K., Cao, C., Chu, H., Zhao, L., Zhao, J., & Lee, X. (2023). Increased heat risk in wet climate induced by urban humid heat. *Nature*, *617*(7962), 738–742. doi: 10.1038/s41586-023-05911-1

Zhao, L., Lee, X., Smith, R. B., & Oleson, K. (2014). Strong contributions of local background climate to urban heat islands. *Nature*, *511*(7508), 216–219. doi: 10.1038/nature13462

Zhao, L., Oleson, K., Bou-Zeid, E., Krayenhoff, E. S., Bray, A., Zhu, Q., . . . Oppenheimer, M. (2021). Global multi-model projections of local urban climates. *Nature Climate Change*, *11*(2), 152–157. doi: 10.1038/s41558-020-00958-8

Zhao, W., Zhang, N., Sun, J., & Zou, J. (2014). Evaluation and parameter-sensitivity study of a single-layer urban canopy model (SLUCM) with measurements in Nanjing, China. *Journal of Hydrometeorology*, *15*(3), 1078–1090. doi: 10.1175/JHM-D-13-0129.1

Zheng, Z., Zhao, L., & Oleson, K. W. (2021). Large model structural uncertainty in global projections of urban heat waves. *Nature Communications*, *12*(1), 3736. doi: 10.1038/s41467-021-24113-9

Zhou, X., Yamamoto, M., Yan, S., Ishida, Y., Cai, M., Ji, Q., . . . Li, C. (2022). Exploring the impacts of heat release of vehicles on urban heat mitigation in Sendai, Japan using WRF model integrated with urban LCZ. *Sustainable Cities and Society*, *82*, 103922. doi: 10.1016/j.scs.2022.103922

Zonato, A., Martilli, A., Di Sabatino, S., Zardi, D., & Giovannini, L. (2020). Evaluating the performance of a novel WUDAPT averaging technique to define urban morphology with mesoscale models. *Urban Climate*, *31*, 100584. doi: 10.1016/j.uclim.2020.100584